

A comprehensive study of the radio properties of brightest cluster galaxies

M. T. Hogan,^{1,2,3★} A. C. Edge,¹ J. Hlavacek-Larrondo,^{4,5,6} K. J. B. Grainge,⁷
 S. L. Hamer,⁸ E. K. Mahony,⁹ H. R. Russell,¹⁰ A. C. Fabian,¹⁰
 B. R. McNamara^{2,3} and R. J. Wilman¹

¹Centre for Extragalactic Astronomy, Department of Physics, Durham University, Durham DH1 3LE, UK

²Department of Physics and Astronomy, University of Waterloo, Waterloo, ON N2L 3G1, Canada

³Perimeter Institute for Theoretical Physics, Waterloo, ON N2L 2Y5, Canada

⁴Kavli Institute for Particle Astrophysics and Cosmology, Stanford University, 382 Via Pueblo Mall, Stanford, CA 94305-4060, USA

⁵Department of Physics, Stanford University, 452 Lomita Mall, Stanford, CA 94305-4085, USA

⁶Département de Physique, Université de Montréal, C.P. 6128, succ. centre-ville, Montréal, QC H3C 3J7, Canada

⁷Jodrell Bank Centre for Astrophysics, School of Physics and Astronomy, The University of Manchester, Manchester M13 9PL, UK

⁸LERMA Observatoire de Paris, CNRS, Université Paris-Sud, F-91405 Orsay, France

⁹ASTRON, Netherlands Institute for Radio Astronomy, Postbus 2, NL-7990 AA Dwingeloo, the Netherlands

¹⁰Institute of Astronomy, Madingley Road, Cambridge CB3 0HA, UK

Accepted 2015 July 7. Received 2015 June 21; in original form 2014 September 12

ABSTRACT

We examine the radio properties of the brightest cluster galaxies (BCGs) in a large sample of X-ray selected galaxy clusters comprising the Brightest Cluster Sample (BCS), the extended BCS and *ROSAT*-ESO Flux Limited X-ray cluster catalogues. We have multifrequency radio observations of the BCG using a variety of data from the Australia Telescope Compact Array, *Jansky* Very Large Array and Very Long Baseline Array telescopes. The radio spectral energy distributions of these objects are decomposed into a component attributed to on-going accretion by the active galactic nuclei (AGN) that we refer to as ‘the core’, and a more diffuse, ageing component we refer to as the ‘non-core’. These BCGs are matched to previous studies to determine whether they exhibit emission lines (principally $H\alpha$), indicative of the presence of a strong cooling cluster core. We consider how the radio properties of the BCGs vary with cluster environmental factors. Line emitting BCGs are shown to generally host more powerful radio sources, exhibiting the presence of a strong, distinguishable core component in about 60 per cent of cases. This core component more strongly correlates with the BCG’s [O III] 5007 Å line emission. For BCGs in line emitting clusters, the X-ray cavity power correlates with both the extended and core radio emission, suggestive of steady fuelling of the AGN over bubble-rise time-scales in these clusters.

Key words: galaxies: clusters: general – galaxies: jets – radio continuum: galaxies.

1 INTRODUCTION

Brightest cluster galaxies (BCGs) occupy an important parameter space within the study of galaxy formation and evolution. Residing spatially and dynamically at the centres of galaxy clusters, they are the most massive galaxies observed and their growth and evolution is intrinsically linked to that of the host cluster (e.g. Tremaine 1990; Lin & Mohr 2007). There is general consensus that a strong evolutionary connection exists between galaxies and the supermassive black holes (SMBHs) at their centres (Magorrian et al. 1998; Silk & Rees 1998, and references therein). The influence of BCG-

hosted active galactic nuclei (AGN) on their surroundings (‘AGN feedback’) persists long after the BCGs’ formation and (major) growth. Understanding the nuclear activity of these galaxies in relation to the wider cluster environment is therefore important. This has important ramifications not only within cluster dynamics and BCG evolution but for comprehending AGN feedback processes globally.

The radiative cooling time at cluster centres is often much less than the Hubble time (e.g. Peres et al. 1998; Voigt & Fabian 2004). This gives an expected cooling rate of 10^2 – $10^3 M_{\odot} \text{ yr}^{-1}$, giving an expected sink of cold material on the order of a few 10^{11} – $10^{12} M_{\odot}$. However, only ~ 1 – 10 per cent of this amount is observed – the classical ‘cooling-flow problem’ (Fabian 1994). Star formation is seen in cooling clusters although typically only at the level required

* E-mail: m4hogan@uwaterloo.ca

to account for a few per cent of gas cooling (O’Dea et al. 2008; Rafferty, McNamara & Nulsen 2008). Similarly, much less cold molecular gas is observed than if cooling dominated (e.g. Edge 2001; Salome & Combes 2003). Additionally there is a deficit of gas seen at intermediate cooling temperatures (e.g. Peterson et al. 2003; Sanders & Fabian 2011) and the central gas temperature fails to cool below ~ 30 – 40 per cent of the ambient temperature at greater radii (Mittal et al. 2009). The AGN action of the BCG is believed to counteract the expected cooling (for reviews see McNamara & Nulsen 2007, 2012; Fabian 2012). This AGN feedback is also used to explain the high mass truncation of the galaxy luminosity function (e.g. Benson et al. 2003; Bower et al. 2006; Croton et al. 2006).

BCG-hosted AGN typically accrete inefficiently, hence their mode of feedback is via ‘maintenance-mode’ (also called ‘low-excitation’, ‘radio-mode’) rather than ‘quasar-mode’ (also called ‘high excitation’; e.g. Heckman & Best 2014, and references therein). Mechanical heating is the favoured method by which energy is coupled from the AGN to the intracluster medium (ICM). Evidence for this AGN feedback is most readily observable through the inflation of cavities by relativistic jets, in the X-ray emitting plasma of many massive clusters (e.g. Fabian et al. 2000; McNamara et al. 2000; Hlavacek-Larrondo et al. 2012a). These cavities, which are often cospatial with extended radio emission, subsequently rise buoyantly increasing cluster entropy and redistributing energy. Detailed studies of local systems have shown that weak shocks (e.g. Randall et al. 2011) and density sound waves (e.g. Fabian et al. 2005) contribute towards energizing the ICM, though they cannot provide enough energy in all systems (Fujita & Suzuki 2005). Observations of large-scale, low surface brightness structures such as radio minihaloes around some BCGs suggest that cosmic rays may also play a role (Pfrommer & Enßlin 2003).

AGN energy from BCGs is sufficient to counteract runaway cooling in cluster cores globally (e.g. Dunn & Fabian 2008). However, this is not always the case for individual sources and the details of the AGN activity cycle and fuelling are uncertain. Often, direct observations of mechanical effects are observationally infeasible thus requiring proxy measures of AGN power.

Radio power correlates with mechanical power for statistical samples, albeit with large scatter (Birzan et al. 2008). However, both the ratio ‘ k ’ (e.g. Willott et al. 1999) of non-radiating particles to synchrotron emitting electrons and the magnetic field are typically poorly constrained, which leads to large uncertainties in conversions between radio emission and mechanical power for individual sources.

An issue that often complicates the study of BCGs (and indeed all galaxies) using radio observations is that the observed emission can be separated significantly in both time and space from the event that created it (e.g. Harwood et al. 2013, for a discussion of spectral ageing). Single-band, often low spatial resolution observations are frequently the only radio information available for a BCG. While these galaxies are then known to be radio-loud, there is large uncertainty both in the physical scale and age of this emission, making multiwavelength comparisons difficult. Observations at a range of spectral frequencies and spatial resolutions are required to overcome this issue. In this paper we use a wide range of data to decompose the radio emission of nearly 300 BCGs into an active component – attributable to current accretion, and an inactive component – attributable to historical accretion. We use these decompositions to link the central AGN activity to the larger cluster environment.

Galaxy clusters can be broadly split into two types. The first, known as ‘cool cores’ (CCs), have short central cooling times (t_{cool}) and strongly peaked X-ray profiles (e.g. Million & Allen 2009). The

second type are more dynamically disturbed, exhibit flatter X-ray profiles and are commonly known as ‘non-cool cores’ (NCCs). Directly measuring t_{cool} , or equivalently entropy, of a cluster is observationally difficult and strongly affected by resolution effects (e.g. Panagoulia, Fabian & Sanders 2014). The presence of line emitting (predominantly $\text{H}\alpha + [\text{N II}]$) filamentary nebulae around BCGs is known to be strongly indicative of the dynamical state of the cluster. Such lines indicate the presence of multiphase gas, and are almost always present only when the central entropy drops below 30 keV cm^2 , equivalent to a $t_{\text{cool}} < 5 \times 10^8 \text{ yr}$ (Cowie et al. 1983; Heckman et al. 1989; Cavagnolo et al. 2008; Rafferty, McNamara & Nulsen 2008; Sanderson, Edge & Smith 2009). These filamentary structures are photoionized by neither the AGN itself nor star formation. Instead they appear to be photoionized by either cosmic rays or hot X-ray plasma penetrating cold gas (Ferland et al. 2009). Alternatively it has been suggested that they may be excited by the reconnection of magnetic field lines trailing in the wakes of rising cavities (Churazov, Ruszkowski & Schekochihin 2013). The presence of these lines can therefore be used as a proxy, with line emitting (LE) clusters corresponding to strongly cooling cores and non-line emitters (NLEs) to either weak- or non-cooling core clusters (see also Crawford et al. 1999).

Overall, this paper looks at the general radio properties of the BCG population as a whole. It uses a large data volume to decompose the radio emission and better understand the radio-loudness of BCGs in relation to the wider environment.

The paper is arranged as follows. In Section 2 we present the sample. Section 3 presents the observations and data. We discuss the radio-spectral energy distribution (SED) decomposition in Section 4. Section 5 considers the monochromatic (L band, $\sim 1.4 \text{ GHz}$) radio properties of the sample. Section 6 considers decomposed radio properties. Sections 7 and 8 contain the discussion and conclusions, respectively. Comments on individual source decompositions, and tabulated data products for data presented for the first time in the current paper, can be found in the appendices that are available in the online version. Unless otherwise stated, we refer to a BCG by use of its host cluster name. We have used a standard Λ cold dark matter (ΛCDM) cosmology with the following cosmological parameters unless otherwise stated: $\Omega_{\text{m}} = 0.3$, $\Omega_{\Lambda} = 0.7$, $H_0 = 70 \text{ km s}^{-1} \text{ Mpc}^{-1}$.

2 THE SAMPLE

2.1 Parent cluster sample

Our parent sample is drawn from three *ROSAT* X-ray selected cluster catalogues – the Brightest Cluster Sample (BCS; Ebeling et al. 1998), the extended BCS (eBCS; Ebeling et al. 2000) and *ROSAT*-ESO Flux Limited X-ray (REFLEX; Böhringer et al. 2004) samples, which contain 206, 107 and 447 clusters, respectively. Since publication some catalogue entries have been reclassified, and there are also a small number of cross-catalogue duplicates. We therefore remove a minority of sources, leaving us with a sample of 199, 104 and 417 sources in the BCS, eBCS and REFLEX samples, respectively. Our total X-ray selected parent sample therefore consists of 720 clusters.

The BCG for each of these clusters has been optically identified and observed spectrally (Crawford et al. 1999; Edge et al., in preparation). The sample was split into those which exhibit optical emission lines (line emitters, henceforth LEs) and those which do not (non-line emitters, henceforth NLEs) (see also Table 1). As mentioned in the Introduction, the presence of these lines is strongly

Table 1. BCGs within the (e)BCS and REFLEX galaxy cluster samples (after removal of ‘contaminant sources’). The samples are broken down both by radio detection in NVSS and/or SUMSS and also the presence of extended optical emission lines around them, which are indicative of the presence of a strong CC.

	Lines	No lines
BCS		
Detected	55	67
Non-detected	8	69
eBCS		
Detected	19	44
Non-detected	6	35
REFLEX-total		
Detected	91	161
Non-detected	17	148
REFLEX-NVSS		
Detected	67	119
Non-detected	10	101
REFLEX-SUMSS		
Detected	36	58
Non-detected	7	55

indicative of the cluster containing a strong CC. It must be noted that their absence is not sufficient to rule out the presence of a weaker cooling core ($5 \times 10^8 \text{ yr} < t_{\text{cool}} < t_{\text{Hubble}}$) but does point towards these clusters being less dynamically settled.

An additional point to bear in mind is that not all clusters contain a single top-ranked BCG, and may instead have two or more similarly sized top-ranked galaxies. In our main sample (MS; see Section 2.2), roughly 5 per cent of our clusters are identified as having multiple BCGs (see Appendices). This is less than the equivalent ~ 15 per cent of the sample of 215 clusters in Crawford et al. 1999 that are claimed to have multiple BCGs. We could therefore be missing a codominant galaxy in some cases, though we note that all clusters were visually inspected in both optical and radio maps and no instances were found of clear unattributed BCGs. Quantifying the effect of unidentified secondary BCGs is difficult. Of the 5 per cent of our sample with multiple BCGs, only one double-BCG system is hosted by a CC cluster (A2627) – both BCGs in this cluster are found to be radio-loud. Only around 30 per cent of the multiple BCGs in NCC clusters host radio-loud AGN, which is less than the approximately 50 per cent of all NCC clusters in our sample that host radio-loud BCGs (see Section 5.2). Whilst clearly circumstantial, and affected by small number statistics, this actually points towards the differences in the radio-loud fraction between CCs and NCCs being higher in systems with multiple BCGs, which would strengthen the results within this paper. The fraction of clusters with multiple BCGs are expected to increase with redshift (e.g. Brough et al. 2002), so should be less of an effect for our sample, which is at low redshift. Overall, we do not believe we are overtly affected by any potential small fraction of unidentified codominant BCGs, although we do caution that this caveat should be considered when interpreting the results.

The BCS/eBCS sky coverage overlaps fully the NRAO VLA Sky Survey (NVSS) radio survey (Condon et al. 1998) (Dec. $> -40^\circ$, complete to ~ 2.5 mJy at 1.4 GHz). Of the 417 REFLEX clusters in our sample, 297 fall within the NVSS region and 156 within the southern sky region covered by the Sydney University

Molonglo Sky Survey (SUMSS; Mauch et al. 2003) (Dec. $< -30^\circ$, complete to ~ 6 mJy for Dec. $< -50^\circ$ and ~ 10 mJy for Dec. $< -30^\circ$ at 0.843 GHz). These subsamples are hereon referred to as the REFLEX-NVSS and REFLEX-SUMSS samples.

36 REFLEX sources fall in the overlap between SUMSS and NVSS. These sources are left in both the REFLEX-NVSS and REFLEX-SUMSS samples when these samples are treated independently. Combining the BCS and eBCS catalogues provides a 303 source subsample that we henceforth refer to as the (e)BCS. The comparable number of clusters in (e)BCS and REFLEX-NVSS allows for self-consistency checks of any found results since the samples were independently compiled.

2.2 Main sample

We have targeted follow-up observations of 246 of these sources at either C- or X- (~ 5 or 8 GHz) band (or both) using the ATCA or VLA (see Appendices A and B). These sources constitute the ‘Main Sample’ (MS) of this paper. They comprise 106 + 64 BCGs (detections+non-detections, respectively) in the BCS, 13 + 2 in the eBCS, 39 + 7 in REFLEX and 9 + 6 additional sources that since publication of the catalogues have been found to fulfil the detection criteria but were not initially classified as clusters. These extra sources are non-detections: A7, A2552, Zw 15, Zw 5029 and Z7833; detections: A11, A291, A1664, A2228 and 4C 05.84. This constitutes follow-up completenesses of 85.4, 14.4 and 11.0 per cent for the BCS, eBCS and REFLEX catalogues, respectively.

Whilst only a minority of eBCS clusters are included in the MS, these were randomly selected from the eBCS prior to its publication and should constitute a fair addition to the MS. The minority of clusters followed up from within the REFLEX sample were selected to be the radio-brightest (*L* band) LE BCGs. The high completeness for BCS provides us with a radio-observed, X-ray selected cluster subsample that is unbiased by any radio priors on the BCGs, which can be tested.

2.2.1 Main sample+

The MS is supplemented using literature values to build SEDs for all BCGs in the parent sample that are radio-matched to at least one NVSS or SUMSS source and have *L*-band fluxes > 15 mJy. We note that the 843 MHz observing frequency of SUMSS is technically below the traditional *L*-band range of 1–2 GHz, however, we refer to both SUMSS and NVSS as ‘*L* band’ for succinctness. Whilst without targeted follow-up, the spectral decompositions of these sources (see Section 4 and Appendix E) contain a higher fraction of upper limits, the addition of these sources does ensure that we are drawing conclusions on the radio behaviour of BCGs from a complete flux-limited sample and immunises us against missing extreme (fainter *or* brighter) objects that may oppose any trends found from the targeted campaign. We refer to this flux-limited sample as the main sample+ (henceforth MS+).

3 OBSERVATIONS

This work has utilized data from a variety of observing campaigns, supplemented by literature measurements.

Both pre- and post-Compact Array Broadband Backend (CABB; Wilson et al. 2011) data from the Australia Telescope Compact Array (ATCA) were analysed, as was VLA data from five observing campaigns (see Table 2). All of these observations followed

Table 2. Breakdown of the ATCA and VLA observations used in this paper that are not previously published elsewhere (All: P.I. Edge). Note that several BCGs are repeated, so these numbers do not correspond to the total number of clusters. See Appendices for full list of sources. This data was used when compiling our SEDs and is presented here for the first time.

Proposal ID	Year	Array	Frequency (GHz)	BCGs observed
C1958	2011	ATCA-6A	5.500	14
C1958	2011	ATCA-6A	9.000	14
C1958	2008	ATCA-6A	4.800	31
C1958	2008	ATCA-6A	8.640	31
AE125	1999	VLA-C	8.435	4
AE125	1999	VLA-C	4.835	80
AE125	1999	VLA-C	1.465	3
AE117	1998	VLA-A	1.385	12
AE117	1998	VLA-A	8.435	32
AE110	1997	VLA-C	4.835	86
AE107	1996	VLA-C	4.835	28
AE099	1994	VLA-C	4.835	24

a standard ‘snapshot’ schedule, with multiple visits to each target source separated by several hours to ensure good hour–angle (HA) coverage. Primary flux calibrators were observed at the beginning and end of each run. Each visit to a science target was sandwiched between short observations of a nearby standard source for phase calibration. Exact calibrators for each source can be found in the online archives.

ATCA and VLA data were reduced and fluxes measured for the detected sources using the Multichannel Image Reconstruction Image Analysis and Display (MIRIAD; Sault, Teuben & Wright 1995) and the Astronomical Image Processing System (AIPS; Greisen 2003) packages, respectively, following the standard reduction procedures.

For the ATCA data, the standard flux calibrator 1934-638 was used in all instances for both absolute gain and bandpass calibration. For the VLA observations, three of the VLA standard flux calibrators (namely 3C 286, 3C 48 and 3C 147) were used, with the actual source used for each observing block dependent on observability. For VLA data sets with more than one frequency channel per spectral window, these sources could also be used for bandpass calibration in most cases. However, in a couple of instances the primary calibrator appeared slightly resolved (specifically 3C 147 for AE117 and AE125 at X band) and so an alternate, unresolved bandpass calibrator was chosen from amongst the phase calibrators for that particular run.

Literature searches were performed, and SEDs populated, for all sources in the MS and its extension. Data were taken from the major radio catalogues [e.g. Australia Telescope 20 GHz Survey (AT20G), Murphy et al. 2010; NVSS and Faint Images of the Radio Sky at Twenty-cm (FIRST) at 1.4 GHz, Condon et al. 1998; White et al. 1997; SUMSS at 843 MHz, Mauch et al. 2003; Molonglo Reference Catalogue (MRC) at 408 MHz, Large et al. 1981; Texas Survey of Radio Sources (TEXAS) at 365 MHz, Douglas et al. 1996; Westerbork Northern Sky Survey (WENSS) and Westerbork In the Southern Hemisphere (WISH) at 325 MHz, Rengelink et al. 1997; De Breuck et al. 2002; TIFR GMRT Sky Survey (TGSS) at 150 MHz; VLA Low-Frequency Sky Survey (VLSS) at 74 MHz, Cohen et al. 2007. Additional fluxes found by searches around the radio-peak coordinates in the NASA/IPAC Extragalactic Database (NED), High Energy Astrophysics Science Archive Research Cen-

ter (HEASARC) data base and/or the National Radio Astronomy Archive (NRAO) were individually scrutinized to ensure matches.

3.1 A note on flux scales

Our ATCA data were calibrated to the Reynolds 1994 flux scale for the standard flux calibrator 1934-638, as calculated in the MIRIAD version 20110127 task ‘MFBOOT’. VLA data were scaled to the standard AIPS version 31DEC11 Perley–Butler scale using the task ‘SETJY’ (see Perley & Butler 2013). Both of these scales are very similar to, but have small improvements over the older Baars scale (Baars et al. 1977). The wide range of literature values uses a range of similar flux standards. This represents an added uncertainty to our SEDs. For data pre-dating the Baars scale (very small number of instances), we have used later determinations re-scaled to the Baars scale. The uncertainties introduced by this range of flux scales should be considered, however, they are much less than those associated with intrinsic source variability and the absolute flux uncertainties, hence should be negligible.

4 SED DECOMPOSITION

4.1 Core versus ‘non-core’

The total radio SED of each BCG can be decomposed into two major components – an active, typically flat spectrum (spectral index¹ $\alpha < 0.5$) component attributed to current activity within the AGN and a typically steeper spectrum component ($\alpha > 0.5$) that comprises all other emission.

The steeper component is most likely to be due to lobe emission and so traces past activity of the central engine. Alternatively it could be due to other acceleration processes towards the centre of the galaxy cluster in which the BCG resides, such as sloshing giving rise to a minihalo or phoenix relics (e.g. van Weeren, Röttgering & Brüggén 2011; ZuHone et al. 2013; Walker, Fabian & Sanders 2014, and references therein). The specific morphological and energetic nature of this component is often difficult to determine and a large variety of nomenclature for the various source types has arisen (see Kempner et al. 2004, for a detailed review). The steep spectrum means that this component becomes less prominent towards higher frequencies and is often faint at L band (~ 1.4 GHz) and above, rendering it difficult to detect if an active core component is present. Conversely, current AGN activity manifesting itself as a flat spectrum core component can be swamped at lower frequencies. High-resolution observations are required at low frequency to properly characterize these components. However, in this work we wish to address the difference in radio emission between ongoing core activity and older, steep spectrum emission. We use ‘non-core’ as an umbrella term to refer to the steeper spectrum component not associated with ongoing core activity, regardless of physical origin and spatial resolution.

The core component may show a synchrotron self-absorption turnover at \sim few GHz but tends to remain flat (or, less commonly, rising) out to several tens of GHz. Similarly the ‘non-core’ component may show a turnover, albeit at much lower ($<$ a few hundred MHz) frequencies. This is more likely to be attributable to free–free absorption. Additionally, this component may exhibit a steepening index at higher frequencies due to synchrotron ageing of the underlying electron population.

¹ Where flux $\propto \nu^{-\alpha}$.

4.1.1 A note on non-AGN related cluster radio emission

When present, both cluster scale radio haloes and peripheral relics (also known as ‘radio gischt’; e.g. Giacintucci et al. 2011a) are excluded from our non-core component, as these are both unrelated to the current AGN activity of the BCG (e.g. Feretti et al. 2012; Brunetti & Jones 2014). There are however a number of other radio structures seen in cluster cores such as minihaloes and phoenix relics whose relationship to the BCG and the cooling core is more uncertain (e.g. Gitti, Brunetti & Setti 2002; Gitti, Feretti & Schindler 2006; Gitti et al. 2007). There is debate in the literature as to the true nature of so-called ‘minihaloes’ and these present a somewhat contentious middle ground between cluster-related and AGN-related radio emission. True minihaloes tend to be reasonably spherically symmetric, steep spectrum, low surface brightness sources that are a few 100 kpc in diameter and centred on the BCG (e.g. Burns et al. 1992; Owen, Eilek & Kassim 2000; Giacintucci et al. 2014b). The electron diffusion lifetime is so long as to exclude acceleration by the central AGN. The emitting particles must therefore be accelerated in situ and appear to be related to the cooling flow. It is however possible (and indeed likely) that the seed population originates in the AGN.

Confusingly, it appears that BCGs often contain a smaller (<few 10s kpc), amorphous halo or ‘confined cluster core’ (e.g. Venturi, Dallacasa & Stefanachi 2004) that appears to be related directly to confined, ageing AGN ejecta. This is also occasionally referred to as a minihalo. As the exact nature of the non-core emission is not paramount for our purposes, we may include in our non-core measures emission that could reasonably be called ‘minihalo’ in the literature, if it contributes a portion of the flux in low-resolution observations that provide such a measurement as the ‘BCG flux’.

4.2 SED fits

The majority of sources were unresolved at the resolution limit of our observations (typically around 4 arcsec at C band, equivalent to ~ 8 kpc at our median redshift). Where core and non-core components were morphologically distinct, individual SEDs were produced and fitted directly for each component.

Sources that remain unresolved on few arcsecond scales could consist of an active core only or small scale yet ageing non-core emission. When very long baseline interferometry (VLBI) observations were available, the ratio of milliarcsecond to arcsecond scale flux could be used to determine if any flux was resolved out on intermediate scales, and what fraction of the flux was truly associated with the core. For sources that are unresolved on few arcsecond scales but for which VLBI observations are not available, variability and spectral shape were used to perform a breakdown of the SEDs on a case-by-case basis (see below). Where a strong case could not be made for unresolved sources being either core or non-core dominated, conservative assumptions were employed.

4.2.1 Main sample

Four simple models were considered for each source SED – a single power law of the form

$$S = A_0 \nu^{-\alpha}, \quad (1)$$

a split power law of the form

$$S = A_0 \nu^{-\alpha_1} + A_1 \nu^{-\alpha_2}, \quad (2)$$

a ‘dropline’ model, which allows for a high-frequency rollover to simulate synchrotron ageing:

$$S = A_0 \nu^{-\alpha} \left(1 - A_1 e^{-\frac{\nu_0}{\nu}} \right), \quad (3)$$

or a gigahertz peaked source (GPS)-like model that allows for a spectral peak to simulate self-absorption (Oriente & Dallacasa 2014):

$$\log(S) = A_0 + \log(\nu)(A_1 + A_2 \log(\nu)), \quad (4)$$

where S denotes measured flux and ‘A’s are constants to be determined.

These fits are not intended as physical models. Indeed it is clear that for the dropline model, extrapolation outside of the region being considered would lead to negative predicted flux. Instead they are merely phenomenological fits to the known data that provide a decomposition of the two radio components – core and non-core.

The single power law provides the simplest possible fit, and often had to be employed for poorly sampled SEDs. The index of this power law was considered, with a flat or inverted slope leading to the detection being attributed to a core component, or a steep slope meaning the detection was classed as a non-core. The nominal cut-off between these distinctions was taken as $\alpha = 0.5$. However, anything flatter than $\alpha = 0.8$ or steeper than $\alpha = 0.2$ was further scrutinized. Maps were visually searched for physical extension at each observed frequency. Variability was considered to indicate the presence of a powerful core, with the proviso that this component is more likely to vary on shorter time-scales. In situations where there was strong evidence for one component dominating the observed flux and hence spectral shape, then the value of this component was taken as a measurement of that component. A limit was placed on the other component by extrapolating with a representative steep ($\alpha_{\text{non-core}} = 1.0$, see Section 4.3) index from the lowest observed frequency or with representative flat ($\alpha_{\text{core}} = 0.2$, see Section 4.3) index from the highest observed frequency for non-core and core limits, respectively.

Where a clear spectral break could be seen (e.g. see panel b, Fig. 1), a split power law was employed to fit the two components. Highly variable sources could display an apparently split spectrum if observations taken at different frequencies were substantially separated in time. Time-scales and any variations between observations at different frequencies were used to help distinguish between consistent and apparent spectral breaks.

SEDs that exhibited the high-frequency rollover typical of an ageing electron population were fit with a dropline model. When only this component was apparent in an SED, the value derived was attributed to the non-core component and a limit placed on the core (e.g. panel c, Fig. 1).

Somewhat unexpectedly, a minority of sources exhibited a strongly inverted, peaked spectrum. These spectral components were fitted using the GPS-like model. This spectral shape is typical of a GPS source, commonly interpreted to be either a young or recently retriggered AGN and as such is indicative of a strong, active core (O’Dea 1998). However in a couple of cases a steep spectrum, low-frequency ‘tail’ of emission can also be seen in the SED, allowing the non-core component to also be measured (e.g. panel a, Fig. 1). Where only a GPS-like component was apparent in an SED, a value was taken for the core and a limit derived for the non-core component (e.g. panel d, Fig. 1).

During the fitting, consideration was also given to the possibility of flux on spatial frequencies not sampled by observations and hence effectively ‘resolved out’. We checked the ratio of peak flux to

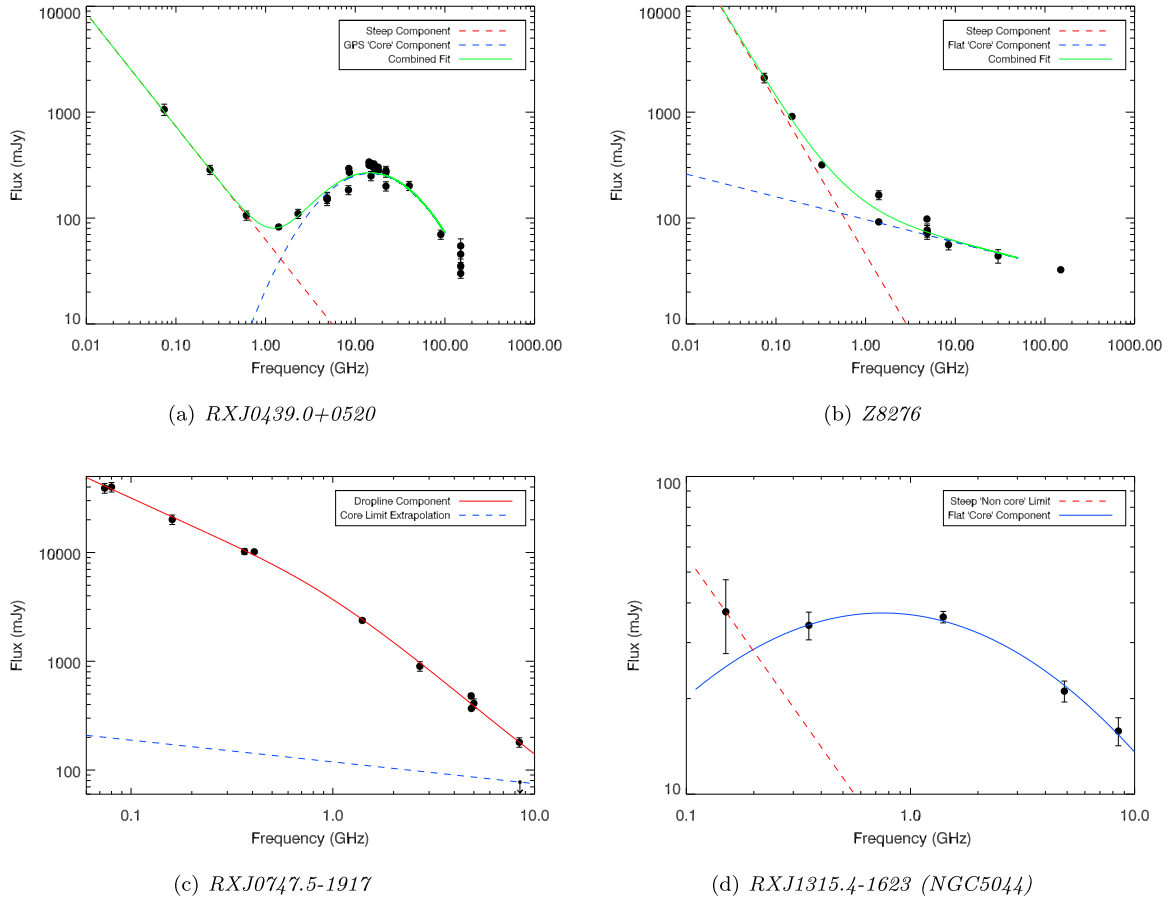


Figure 1. Example SEDs for four different source types. In panel (a), RX J0439.0+0520 is dominated by a GPS-like core component at frequencies above ~ 1 GHz although a clear steep spectrum component is seen at lower frequencies. Panel (b) shows Z8276 where such a dominant inverted core is not present yet there is still a distinct flattening of the spectral index to higher frequency suggestive of a significant active component in the system. This appears well represented by a split power law. Not all sources can be fit with two distinct components. Panel (c) for example shows RX J0747.5–1917, which appears to be well fit by a steep power law with a rollover to higher frequencies (i.e. a ‘dropline’, see text). This source is slightly resolved at X band with the VLA-A, hence extrapolating from the peak of this observation allows an upper limit to be placed on a core contribution. Alternatively, panel (d) shows RX J1315.4–1623 whose BCG is unresolved at all observed frequencies and exhibits a peaked SED, indicative of it being dominated by an active, self-absorbed core. There is a map detection at 150 MHz from TGSS that may indicate the presence of a weak non-core component although the uncertainty is too large to derive a high-quality measurement and hence a limit on the non-core is derived by extrapolating from this low-frequency point. [A colour version of this figure is available in the on-line journal.]

flux extracted using a single Gaussian fit (AIPS task JMFIT) for sources that appeared unresolved. Furthermore, where possible the flux ratio between two unresolved observations of a source at the same frequency but different spatial sampling was taken (e.g. FIRST/NVSS at 1.4 GHz). In truly unresolved sources, both of these ratios should give unity. Of course it should be noted that variability could also affect these ratios. Again, caution was employed to ensure that such effects did not overly bias our breakdowns.

Full details of the breakdowns for each source in the MS can be found in Appendices A–C. All SEDs are available online Hogan 2014.

4.2.2 Main sample+

For some brighter members of the MS+ extension (e.g. Hydra A and Hercules A) clear morphological decompositions were possible. Where this was not the case, spectral breakdowns were performed using the same criteria as for the MS with the exception that, due to the typically much lower spectral coverage and less available data, GPS-like and dropline models were not used as they were

poorly constrained. Often a single index fit around the normalization frequency had to be taken.

For many of the sources in the MS+ extension, radio coverage was limited to only the *L*-band detection. In these instances the detection thresholds of higher frequency large-scale surveys, predominantly the Green Bank 6-cm at 4.85 GHz (GB6; Condon et al. 1994), the Parkes–MIT–NRAO surveys at 5 GHz (PMN; Griffith & Wright 1993) and AT20g were considered to determine whether the source has a flatter spectrum component to high frequencies or whether the *L*-band flux is attributable to a dominant non-core. Where a limit on a higher frequency flux determined that the *L*-band detection must be due to a source with spectral index $\alpha > 0.8$ then it was attributed to dominant non-core emission and an estimate of this made using a short extrapolation with $\alpha_{\text{Steep}} = 1.0$. Core limits were then drawn using $\alpha_{\text{Flat}} = 0.2$. These indices were chosen on the basis of being typical of the α s found for clearly identifiable components.

When the higher frequency limits did not constrain spectra to be flatter than $\alpha = 0.8$ caution was employed and limits taken on both components, extrapolating from the *L*-band detection with indices $\alpha_{\text{Steep}} = 1.0$ and $\alpha_{\text{Flat}} = 0.2$ for the steep and flat components,

respectively (see also Section 6). Similarly, lower frequency survey limits were considered to ascertain whether a lower limit of $\alpha_{\text{Flat}} < 0.5$ could be determined for any sources, so ruling out a source being steep spectrum dominated.

Notes for the decomposition of each SED in the MS+ can be found in Appendices D and E. All SEDs are available online Hogan 2014.

4.3 Measured indices

Figs 2 and 3 show the distributions of measured indices for our MS and MS+, respectively. Whilst (partly by nature of the differentiation criteria) there is a clear split between the flat spectrum core component and the steep spectrum non-cores, some crossover of indices is seen. For the core components, not all will necessarily be flat and exhibit self-absorption. Indeed, for a ‘naked core’ where the base of a recently triggered jet can be seen then an injection index of ~ 0.6 may be expected (Laing & Bridle 2014). Alternatively, extended emission can have a relatively flat spectrum ($\alpha \leq 0.6$). A tail to inverted core spectra is seen, mirrored by a tail to ultrasteep components for non-cores.

Our choice of a representative indices of $\alpha_{\text{core}} = 0.2$ and $\alpha_{\text{non-core}} = 1.0$ for extrapolations initially appear to be slightly too flat and too steep, respectively, when considering Figs 2 and 3. These choices are however governed by conservatism. If we consider the median index for the core and non-core when all measured indices for each of these components are included, we arrive at $\alpha_{\text{core}} = 0.33$ and $\alpha_{\text{non-core}} = 0.96$ (considering the MS only, as this has most reliable index measurements). However, if we restrict our sample to the subset of sources where both a measure of the core and non-core were obtainable our median indices are $\alpha_{\text{core}} = 0.28$ and $\alpha_{\text{non-core}} = 1.08$. Often when a source is detectable out to frequencies above 10 GHz it either contains a clearly identifiable active core component or is a bright source, which in most cases have VLBI measurements. For these reasons in most cases where core extrapolation is required it is from below the 10 GHz normalization. Therefore a flatter index provides a more conservative upper limit, hence our choice of $\alpha_{\text{core}} = 0.2$.

On the other hand, the majority of extrapolations for the non-core component were from below the 1 GHz normalization frequency and hence a flatter index is more conservative. We therefore choose $\alpha_{\text{non-core}} = 1.0$ as our representative index. For cases where an extrapolation of a given component is required we employ uncertainties of $\alpha_{\text{error}} = \pm 0.2$.

The presence of a significant tail of ultrasteep non-cores suggests that such emission may be fairly common around BCGs. Amorphous and minihalo emission is often found to be very steep ($\alpha > 1.5$), suggesting there may be a link between these structures and emission from a persistent AGN.

For sources not detected in our pointed observations, literature searches were performed to determine whether there was any weak, steep spectrum emission present at lower frequencies. Limits on both the core and non-core components were determined by extrapolating with representative indices from the relevant survey limits.

5 MONOCHROMATIC L-BAND RADIO PROPERTIES

Initially we consider the flux limited monochromatic radio properties of our parent sample around 1.4 GHz, to gain an overview of the general radio properties.

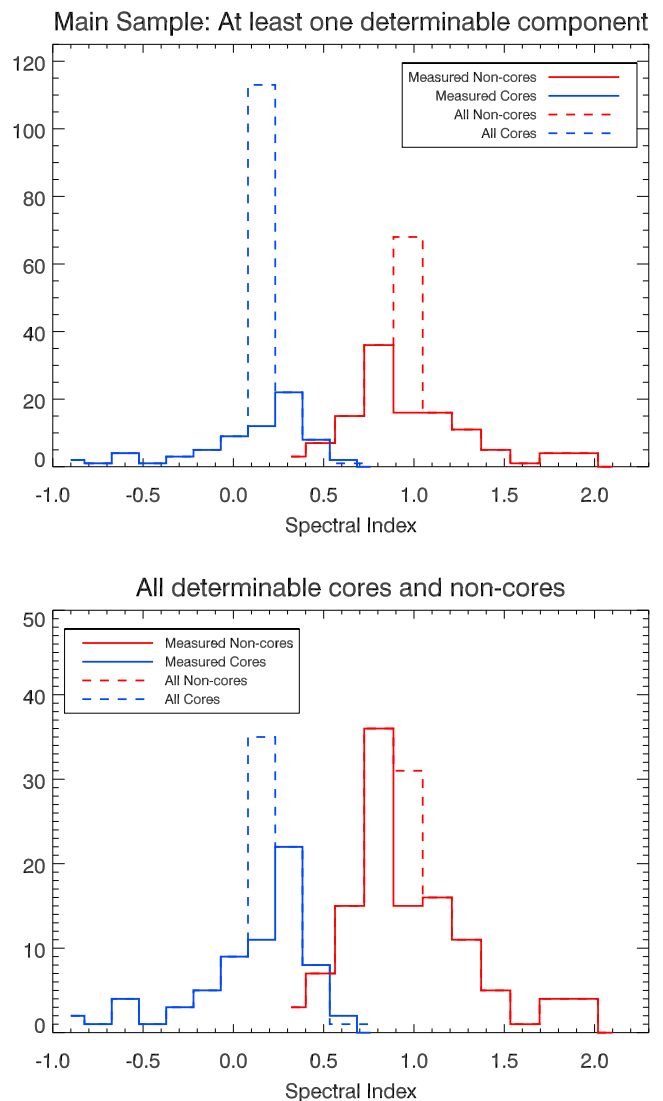


Figure 2. Incidence of fitted indices for the core and non-core fitted components to our MS. In both panels, blue lines represent the fitted index of the core component and red that of the non-core. Solid lines are instances where the relevant component could directly be determined whereas the dotted lines include the components where a representative index had to be assumed ($\alpha_{\text{Steep}} = 1.0$ and $\alpha_{\text{Flat}} = 0.2$, see text for justification). For the top panel, all sources in the MS are included for which at least one component could be measured, hence the high incidence of assumed indices as required for extrapolated limits. In the lower panel, the red lines trace all instances where a core value could be determined and the blue lines trace all instances where a non-core value could be determined. Note that limits remain in the lower panel for when a component could be resolved and had a measurement near to either normalization (e.g. a VLBI core measurement) and only a small but secure extrapolation was required, nonetheless needing an index to be assumed. See also Appendix A. [A colour version of this figure is available in the on-line journal.]

5.1 Radio matching

The optical BCG positions of the entire parent sample were cross-referenced with the NVSS and SUMSS radio catalogues, initially searching within their respective positional uncertainties (1–7 arcsec for NVSS, 1–10 arcsec for SUMSS). Additional uncertainty for the radio source position arises due to the relatively large beam sizes (~ 45 arcsec). Where a radio source was matched to within one

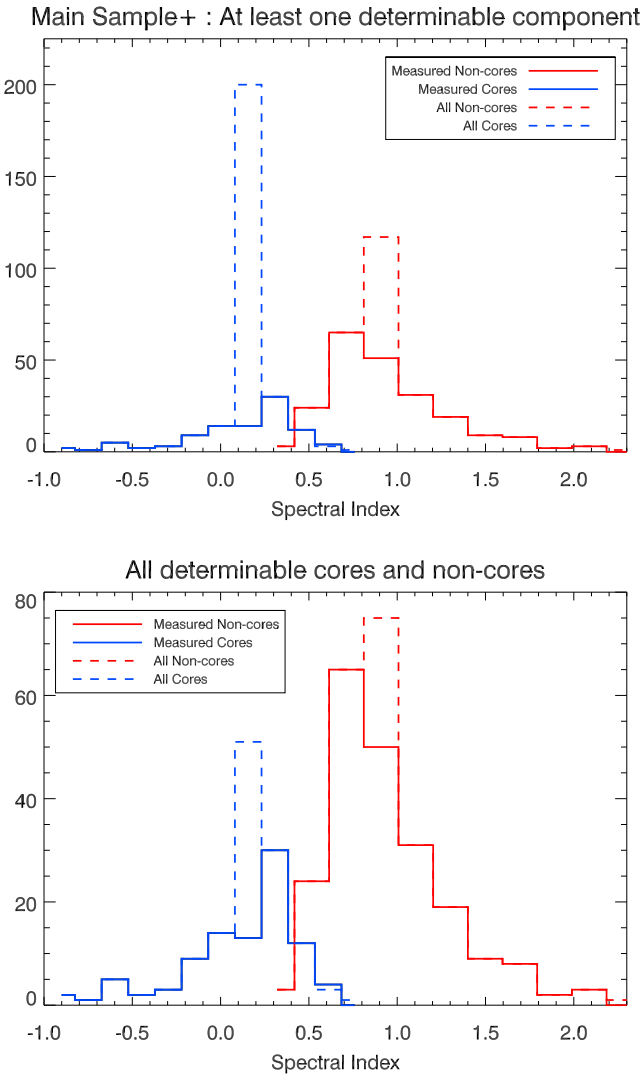


Figure 3. Same as for Fig. 2 except now extended to include the full flux limited MS+. We again include sources with an assumed index as these highlight the ratio of instances where an index could be directly determined to when, even with our relatively good spectral coverage, an index had to be assumed for an individual component. [A colour version of this figure is available in the on-line journal.]

beam size but greater than 2 arcsec from the optical position, the sources were inspected visually to ascertain whether the match was robust. Additionally, where multiple matches fell within the beam size they were visually inspected to ensure multiple components of individual sources were appropriately included.

A sizeable proportion of the (e)BCS clusters (~ 73 per cent) fall within the FIRST (Becker, White & Helfand 1995) survey region (matched to Sloan Digital Sky Survey, Dec. limit > -10), which has a higher resolution (~ 5 arcsec) and lower flux limit (~ 2 mJy) than NVSS. A much smaller portion (~ 26 per cent) of sources within the REFLEX-NVSS sample also fell within the FIRST region. Sources within this overlap region were additionally cross-matched with the FIRST survey and radio-optical overlays were inspected. With the higher resolution data of FIRST, we find that ~ 15 per cent of sources tagged as matches in NVSS were likely not associated with the BCG. It should therefore be noted that the absence of a similarly high-resolution southern survey is likely to introduce a bias in that misattributions of a radio source to the BCG are less

likely to be noticed in the Southern hemisphere. However, we also find that ~ 10 per cent of sources in the FIRST footprint that were not detected by NVSS were either detected with the fainter threshold of FIRST or shown to be radio-loud independently of another nearby source and hence this bias is likely to be tempered by the lower detection threshold and higher resolution of the FIRST survey.

5.2 LE and NLE match rates

The number of BCGs matched to radio sources can be seen in Table 1, along with a breakdown of whether these BCGs are optically LE or NLE. We find detection percentages of 61.1 ± 5.5 , 62.6 ± 5.5 and 60.3 ± 7.7 per cent for (e)BCS, REFLEX-NVSS and REFLEX-SUMSS, respectively, assuming simple binomial errors with a 95 per cent confidence level.

These BCG radio-detection rates are slightly elevated compared to other X-ray selected samples. For example, Sun et al. 2009 found a 50.3 per cent detection rate for a luminosity cut of $L_{1.4\text{GHz}} > 10^{23} \text{ W Hz}^{-1}$ for their sample of 43 nearby galaxy groups with *Chandra* archival data. A ~ 50 per cent detection rate was found for both the Brightest 55 (B55; Edge et al. 1990; Peres et al. 1998) and the Highest X-ray Flux Galaxy Cluster Sample (HIFLUGCS; Reiprich & Böhringer 2002; Mittal et al. 2009) samples. Ma, McNamara & Nulsen (2013) studied a combined sample of 685 X-ray selected galaxy clusters. Matching to the NVSS, they found a matched detection rate between the cluster coordinates and radio sources > 3 mJy of ~ 52.1 per cent (or ~ 48.5 per cent accounting for expected background contamination). Where possible we have used the lower flux detection threshold of the FIRST survey and also matched the optical BCG positions rather than cluster X-ray positions. Considering these factors, we have reasonable agreement with previous radio-BCG detection rates in X-ray selected clusters.

Our detection rate is significantly higher than for otherwise derived samples (e.g. ~ 30 per cent for optical selection; Best et al. 2007; Stott et al. 2012, with BCG mass dependency). This reflects the fact that X-ray selected samples are biased towards selecting the most massive, settled clusters which are more likely to host a radio-loud BCG (Burns 1990; Mittal et al. 2009). However, a fraction of our non-detections are likely to be radio-loud but below our detection threshold and so our detection rate can only provide a lower limit on the overall duty cycle of radio-loudness of BCGs. The misidentification of some clusters that contain central radio sources, due to X-ray emission being incorrectly attributed to the AGN rather than the ICM, may also contribute.

More interesting is the difference in the detection rate between LE and NLE BCGs. We detect 84.1 ± 7.6 , 87.0 ± 7.5 and 83.7 ± 11.0 per cent of the LEs and 51.6 ± 6.7 , 54.7 ± 6.6 and 51.3 ± 9.2 per cent of the NLEs in (e)BCS, REFLEX-NVSS and REFLEX-SUMSS, respectively, again assuming a simple binomial errors with a 95 per cent confidence level. Note that these detection fractions are affected by inconsistent flux limits and that if we instead consider only our C-band pointed observations of the MS BCGs, then we recover detection fractions of 90.8 ± 5.1 per cent for LEs and 48.9 ± 8.8 per cent for NLEs down to our typical detection limit of ~ 0.3 mJy. These detection fractions compare favourably with those of Mittal et al. 2009, who report detection fractions of 45, 67 and 100 per cent for NCCs, weak CCs ($1 < t_{\text{cool}} < 7$ Gyr) and strong CCs ($t_{\text{cool}} < 1$ Gyr), respectively, for the HIFLUGCS sample of the 64 X-ray brightest galaxy clusters.

If the simplest case is taken whereby the detection rate is taken as a proxy for the duty cycle of AGN activity (e.g. Lin & Mohr 2007), then this provides clear evidence that the duty cycle of BCGs in

strong cooling flow environments is higher than for BCGs in less extreme cluster centres.

5.3 Luminosity functions

A further clear distinction in the radio properties between LEs and NLEs becomes apparent by considering their luminosity distributions (see Fig. 4). Radio sources in LE BCGs are on average more powerful than for NLEs. The distributions in Fig. 4 are effectively complete to $\geq \text{few } 10^{23} \text{ W Hz}^{-1}$. Although the distributions in the directly comparable (e)BCS and REFLEX-NVSS samples (Fig. 4, top panel) are not perfectly aligned (see below), the same general result is seen.

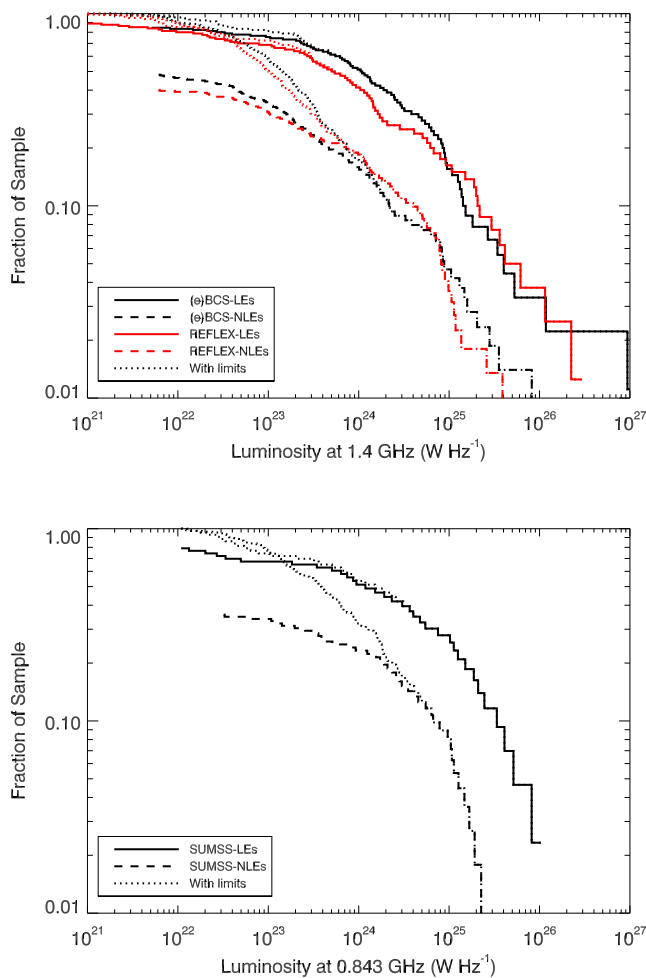


Figure 4. Radio luminosity functions (RLF) for all BCGs within the (e)BCS and REFLEX-NVSS (top panel) and REFLEX-SUMSS (bottom panel) X-ray selected catalogues, separated by the presence of extended optical emission lines. In both figures, solid lines trace LEs, dashed lines trace NLEs and dotted lines trace upper limits for galaxies that are radio-faint to the detection limit of the relevant survey. A clear environmental dependence is seen for LEs to host more luminous sources. The top panel shows the 1.4 GHz RLF for all clusters that lie within the NVSS survey region for both the (e)BCS catalogue and REFLEX catalogue, with the relations for the two surveys showing good agreement and repeatability of the result. The bottom panel shows the 0.843 GHz RLF for clusters in the REFLEX catalogue which fall within the SUMSS survey region. [A colour version of this figure is available in the on-line journal.]

5.3.1 Redshift considerations

Differences in the redshift distributions of clusters in the two samples may account for some of this scatter. Malmquist bias would give preference for detecting higher luminosity sources in a sample with a higher redshift distribution. The redshift distributions of the clusters with radio-loud BCGs for the three subsamples are shown in Fig. 5, with 1σ uncertainties assuming Poissonian errors. There is no significant difference in the redshift distribution of our LE and NLE BCGs. For the REFLEX sample, to low significance there are proportionally more LE BCGs in the lowest redshift bin ($z < 0.1$). However, this would suggest a higher redshift distribution for our NLEs than LEs and should therefore be expected to bias our NLE sample to be more luminous than LEs. Hence such a bias, if present, actually serves to strengthen our result. To minimize any redshift related uncertainty, the distributions were replotted for only those clusters at $z < 0.1$ (see Fig. 6). The distributions between the (e)BCS and REFLEX-NVSS samples now appear to agree with less scatter and the trend for LEs to host more powerful radio sources remains.

It should be considered that there is a decreasing fraction of strong CCs observed to higher redshift, although this evolution is not believed significant over the redshift range of our sample (Santos 2010; Samuele et al. 2011; McDonald et al. 2013a).

There were 36 matched BCGs within our sample which lie in the overlap of the NVSS and SUMSS regions. This relatively small sample was found to have a reasonably uniform range of $\nu_{0.843 \text{ GHz}} - \nu_{1.4 \text{ GHz}}$ indices of $\alpha = -0.27$ – 2.12 . This range of indices highlights the wide diversity of radio activity found within the BCG population. It also highlights the large uncertainties that are invoked by assuming a single spectral index for a population of sources when extrapolating too far from a single frequency observation. As such we do not extrapolate the REFLEX-SUMSS sample to 1.4 GHz for direct comparison (Figs 4 and 6) and instead note only that the luminosity distinction between LEs and NLEs remains.

5.4 Cluster X-rays to L -band radio connection

To further investigate how the radio behaviour of the BCG connects with the global properties of the host cluster we retrieve the integrated cluster X-ray emissions from the BCS, eBCS and REFLEX catalogues. Table 6(a) of the REFLEX catalogue contains the X-ray luminosities calculated using our cosmology. However, the BCS and its extension both give X-ray luminosities for an Einstein–de Sitter universe with $H_0 = 50$. We correct this to our cosmology, with typical conversion factors of 0.5–0.7 for our redshift range. We show in Fig. 7 the monochromatic L -band radio powers for all sources in our parent sample as a function of the X-ray luminosity of their host clusters. A general trend for the highest radio luminosity sources to inhabit the most X-ray luminous clusters is seen, albeit with significant scatter. The extended nature of clusters means that the catalogue observations sample regions of much greater physical extent than just the cluster core. The integrated X-ray luminosity is therefore driven predominantly by the cluster mass, with more massive clusters corresponding to more X-ray luminous systems. The correlation observed in Fig. 7 is therefore indicative of the most massive clusters tending to host the most powerful radio AGN, which may itself be due to more massive clusters hosting more massive BCGs and in turn more massive central black holes. A secondary effect, for CC clusters to have elevated X-ray luminosities due to the higher core densities could also be contributing. However this

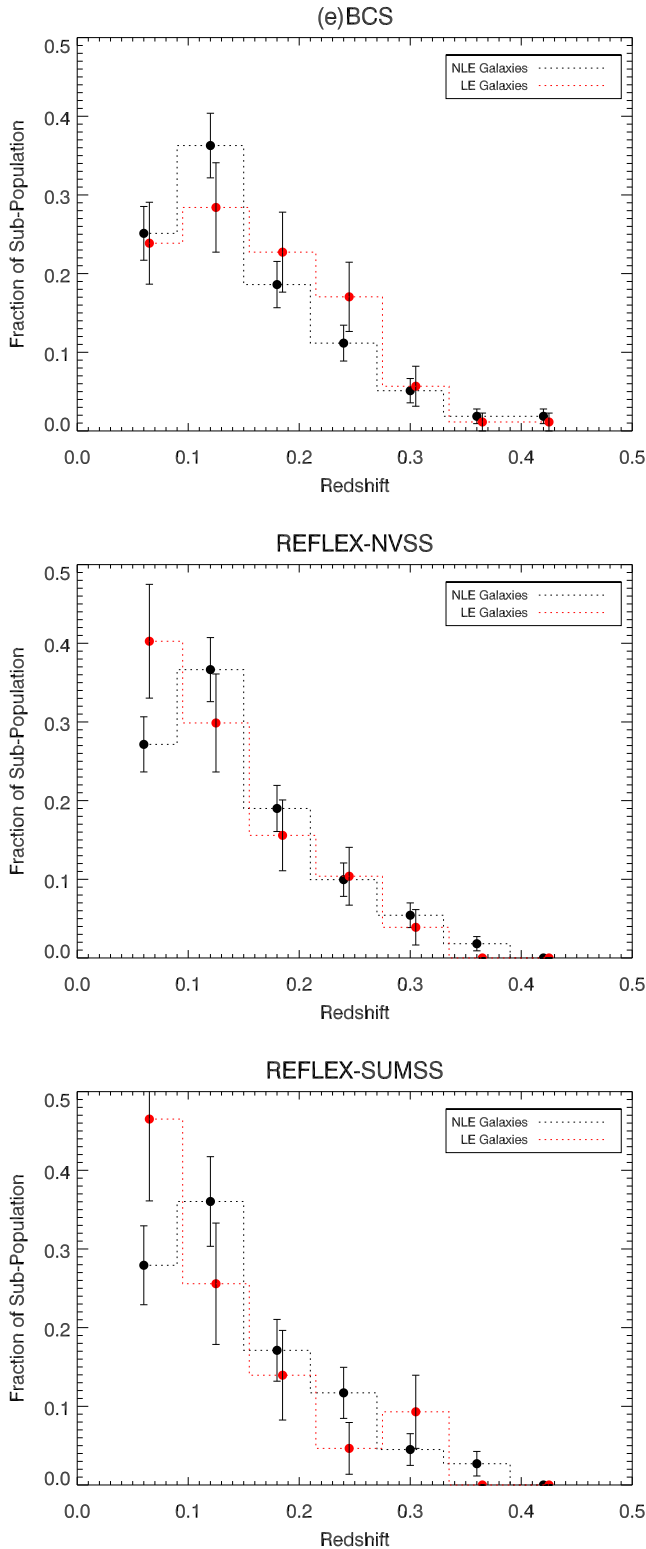


Figure 5. Binned redshift distributions for the radio-matched BCGs within the (e)BCS (top panel), REFLEX-NVSS (middle panel) and REFLEX-SUMSS (bottom panel) samples. [A colour version of this figure is available in the on-line journal.]

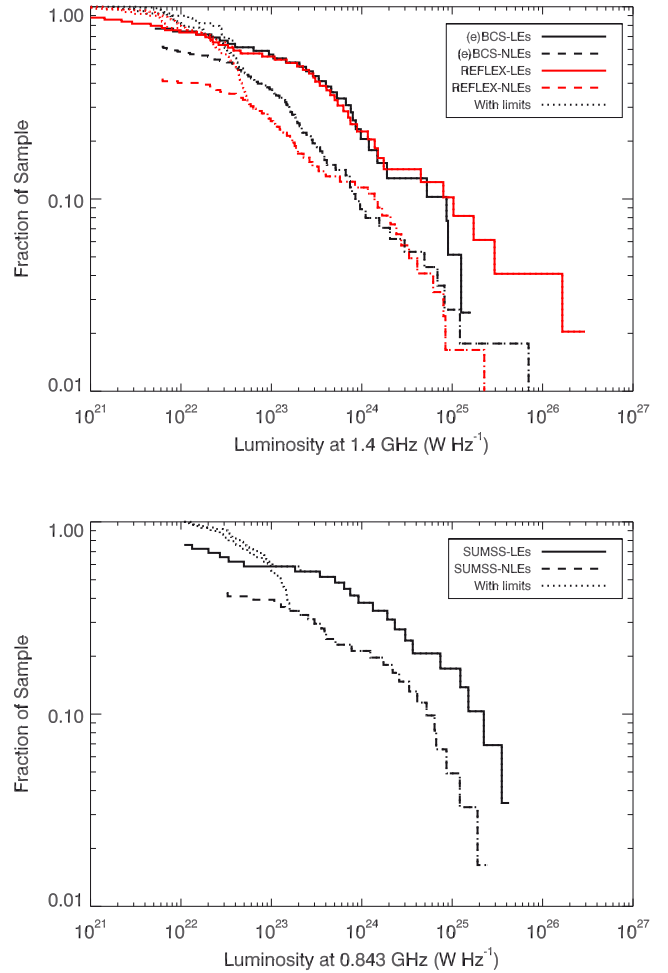


Figure 6. As for Fig. 4 although restricted to $z < 0.1$ clusters. We see that the result remains, showing that it is a true physical result and not merely due to redshift bias. In particular note that the relations for (e)BCS and REFLEX-NVSS now appear to align better. Better identification of sources in REFLEX covered by NVSS but not FIRST at lower redshifts could account for this. [A colour version of this figure is available in the on-line journal.]

is likely to be a much more subtle effect than the mass dependency and is not the dominant driver of the correlation.

6 CORE AND NON-CORE EMISSION

As stated in the Introduction, the true nature of any observed radio activity is difficult to understand when observing a sample at only one frequency. We now consider the properties of the decomposed core and non-core radio components, their relationship to each other and their separate and linked relationships to other cluster and AGN properties.

6.1 Linked emission

For each of the sources within the MS, we take monochromatic proxy measures of the core and non-core components at 10 and 1 GHz, respectively. Ideally, the cores would be normalized at a higher frequency and non-cores at a lower frequency. However, often our radio SEDs are more sparsely sampled far away from the traditional cm-range wavelengths. Hence, our choice of 10 and 1 GHz for the normalizations is a compromise between ensuring

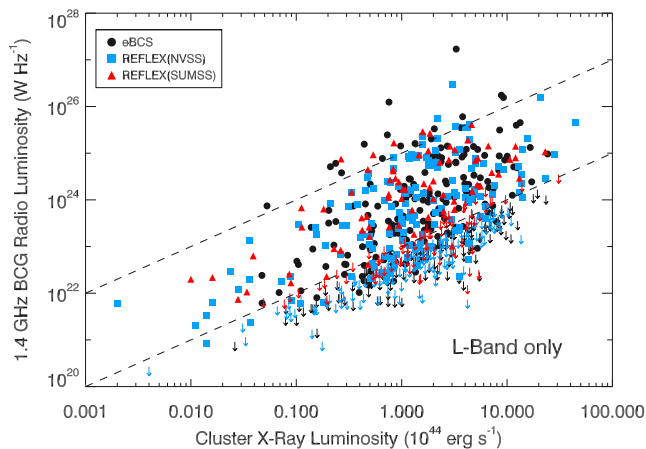


Figure 7. Monochromatic (1.4 GHz) radio luminosity of the BCG as a function of its cluster’s luminosity. The empty corner to the bottom right reflects the detection limit of the radio surveys rather than a true correlation whereas the bound to the upper-left shows that more radio-luminous BCGs tend to inhabit more X-ray luminous clusters. Note that REFLEX-SUMSS radio fluxes were extrapolated using an index of -0.8 for inclusion/completeness. See Section 5.3.1 for why this extrapolation is uncertain. X-ray luminosities were corrected to the same cosmology. The dashed lines are illustrative only and represent one-to-one normalization with a two order of magnitude separation. [A colour version of this figure is available in the on-line journal.]

the relevant components can be separated whilst still being within the best-sampled section of the radio waveband. We plot a radio ‘colour-colour diagram’ of the 10 GHz core normalization against the 1 GHz non-core normalization in Fig. 8.

Both cluster types can host powerful radio sources, yet BCGs in strongly cooling clusters are much more likely to be core dominated. To further elucidate this difference in distribution, in Fig. 9 we plot a histogram of the ratio of the 10 GHz core measure to the 1 GHz non-core measure for the sources in the MS that have well determined values for *both* components. As in Fig. 8, we see a tendency for LEs to host much more core dominated radio sources.

Strong core components only appear to be found in LEs. The presence of very powerful non-cores in NLEs, normally associated with classical Fanaroff–Riley type I (FR-I) and type II (FR-II) sources, belies that there must at some times be powerful core activity in these objects. It stands to reason that in a much larger sample we would find such events. However, that they are not present in the current sample suggests that such core outbursts must be short-lived. Indeed we find that for the 48.8 per cent of sources that are identified as LEs in our MS, 60.2 per cent have a determinable core component of which 83.1 per cent are more powerful than $10^{23} \text{ W Hz}^{-1}$ at 10 GHz (see also Section 7.1). However, of the remaining 51.2 per cent of sources tagged as NLEs only 11.6 per cent have an identifiable core component. Only 5 per cent of these NLE core components are more powerful than $10^{23} \text{ W Hz}^{-1}$ at 10 GHz and none has a core power above $5 \times 10^{23} \text{ W Hz}^{-1}$ (see also Section 7). This suggests an upper limit to the *core* duty cycles of NLEs of <1 per cent with core powers greater than $5 \times 10^{23} \text{ W Hz}^{-1}$ whereas the prevalence of powerful core activity is much higher and more persistent, in LEs. It is the presence (or lack) of an active *core* component that appears to be the most important distinction between the radio properties of LE and NLE BCGs, even more so than their overall incidence of radio-loudness (see Section 5.2).

The wide range of ratios of these two components has important implications for the variety of sources that will be contained

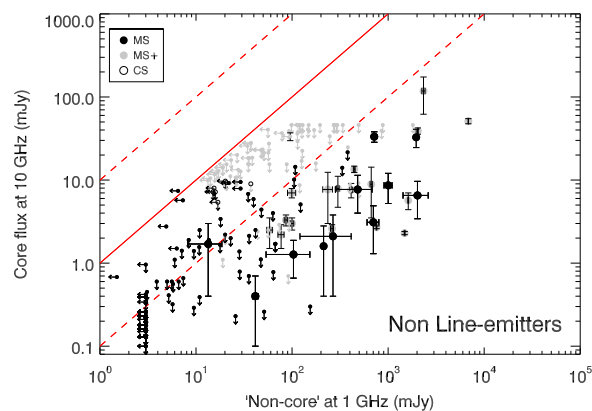
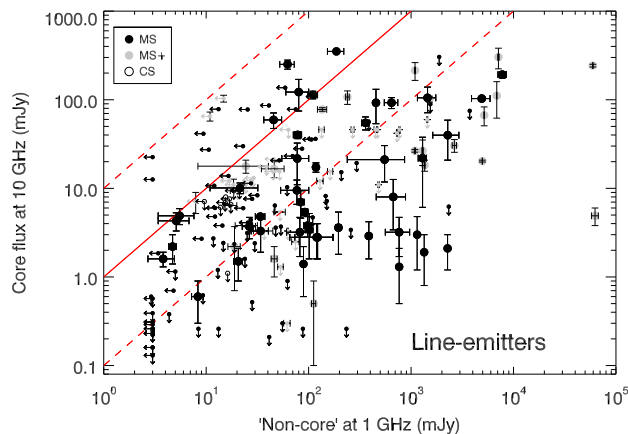


Figure 8. Comparison of the flux density of the radio core component (normalized at 10 GHz) to that of the more diffuse radio component (normalized at 1 GHz) for those objects that exhibit optical line emission (top) to those that do not (bottom). The solid line marks equal normalization of both components, the dashed lines a factor of 10 either side. It appears that LE clusters are significantly more likely to be core-dominated radio sources whilst also undergoing the most powerful events. Solid grey points in both plots are sources in the MS+ ($L_{\text{band}} > 15 \text{ mJy}$) which are not covered by the MS (see text). Open symbols complete the radio coverage down to the flux limit of the SUMSS survey ($15 > S_{L_{\text{band}}} > 10 \text{ mJy}$) and hence occupy only a narrow range in flux density. [A colour version of this figure is available in the on-line journal.]

within any flux selected radio sample, with samples selected at different frequencies containing vastly different source types. This is discussed in Section 7.4

6.1.1 Complete sample

To ascertain whether our MS is representative of the full parent sample, in Fig. 8 we also show (in light grey) the decompositions for all sources in the MS+ that do not fall within the MS.

Considering the top panel of Fig. 8 we see that for the LEs, the MS (black points) well samples the parent sample. For the NLEs (bottom panel) it initially appears that many grey points lie above the black points. Almost all of these are shallow upper limits on the core component for sources where there is no indication of a strong active core. Sources in the MS are similarly spread in non-core flux but have deeper limits on the core components from the targeted observations at higher frequencies. It therefore appears reasonable to assume that the advent of deeper higher frequency surveys (e.g. AT20G deep; Franzen et al. 2014) will push the MS+ core limits

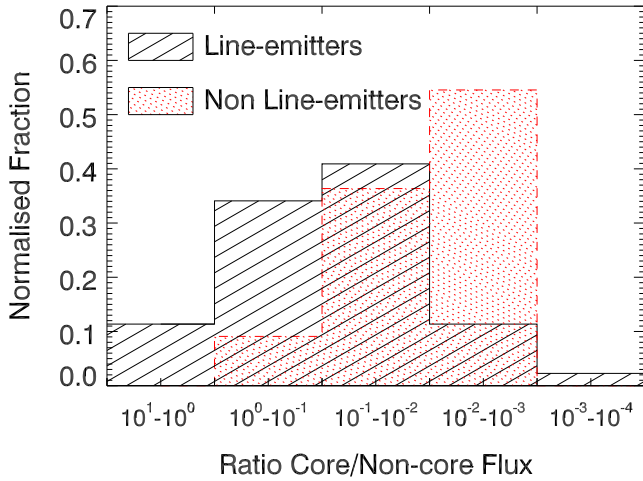


Figure 9. Distribution of the core to non-core ratio of normalizations for the sources in the MS only, that have determined values for both components. This subsample of data is incomplete yet represents the most well sampled of the data displayed in Fig. 8 and highlights that LE-BCGs are on average much more likely to host core-dominated radio sources than NLEs. [A colour version of this figure is available in the on-line journal.]

down. We therefore believe that the MS for NLEs is indicative of the true distribution of the parent sample.

Note that although the limits on NLEs in the MS+ core components do tend to lie above the limits on the corresponding points in the MS, they are still all below the brightest cores seen in LEs.

For completeness, we also include in Fig. 8 *approximate* positions for the remaining sources in the parent sample that have *L*-band radio fluxes between 10 and 15 mJy. This is the level to which *all* the *L*-band surveys used are complete. This is referred to as the completeness sample (CS) in the image, and these points do not appear to lie anywhere special on the diagram.

6.2 Cluster X-rays to decomposed radio connection

For the full MS+ sources, we plot the luminosity of their core and non-core radio components against their cluster X-ray luminosities in Fig. 10. Whilst there appears to be a general tendency that the most powerful cores only occur in the most X-ray luminous clusters, there is a population of powerful non-cores ($>10^{24}$ W Hz $^{-1}$) found in low X-ray luminosity ($<5 \times 10^{43}$ erg s $^{-1}$) clusters. In the simplest scenario it would be expected that bright cores should evolve into bright non-cores. The lack of bright cores alongside the presence of bright non-cores in low X-ray luminosity clusters is inconsistent with this simple picture, hence we must consider alternate explanations for the bright non-cores.

6.2.1 Activity cycle considerations

Whilst strong non-cores can be the result of either the superposition of multiple previous periods of activity or the fading of a single powerful outburst, a powerful core can only be observed as the result of strong, current activity. Powerful non-cores in low X-ray luminosity clusters could therefore be explained by a couple of different scenarios. Individual periods of core activity may be genuinely less powerful in less X-ray luminous clusters but happen relatively frequently, thus leading to a build-up of material. Alternatively, powerful core outbursts may occur in low X-ray luminosity clusters yet be relatively rare and simply missed by our sample.

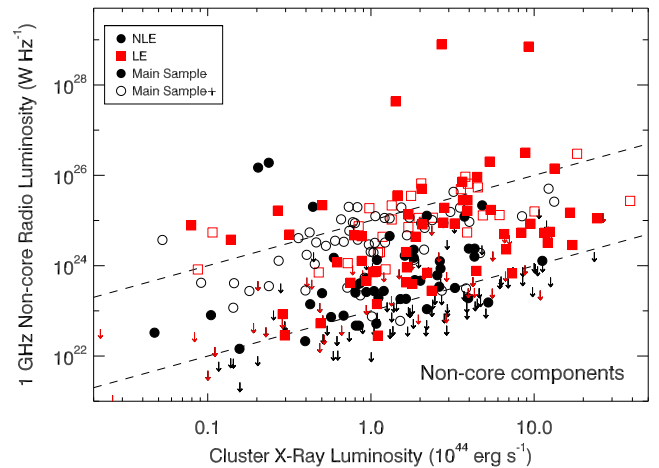
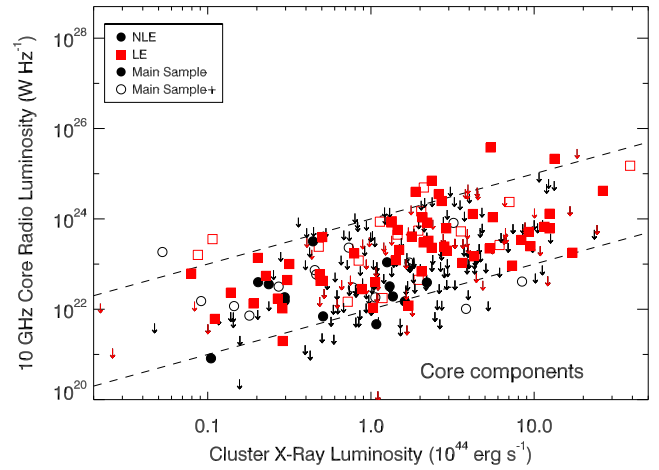


Figure 10. Relationship between the core (top) and non-core (bottom) radio components of the BCG to the overall X-ray luminosity of the host cluster. Note that the strongest cores appear only to occur in the most X-ray luminous and hence most massive clusters whereas strong non-cores, attributable to single outburst lobe-dominated systems may also be found in low X-ray luminosity clusters. Black points are NLEs whereas red points are LEs. The dashed lines are illustrative only and represent one-to-one normalization with a two order of magnitude separation. [A colour version of this figure is available in the on-line journal.]

The former of these two possible explanations could potentially explain the observed ‘amorphous haloes’ observed around many BCGs (e.g. A2052; Blanton et al. 2001; Venturi et al. 2004), and of which our current sample contains several candidates (e.g. A2627, A407, AS753, AS861, RX J1720.1+2638; also see Appendix A). This halo would contain multiple distinct populations of electrons from a number of previous outbursts, all at different stages of ageing but crucially none of which would be undergoing injection and hence manifest as an active, flatter spectrum core. In this scenario, the superposition of weak populations would build to give the overall bright non-core. High-resolution spectral index maps of amorphous haloes could support this, if the distribution of the spectral index across the haloes was found to be clumpy rather than smoothly varying. Resolution effects at the varying frequencies would however make such an endeavour difficult.

To attempt to break the degeneracy between single outburst and accumulated non-cores, we considered the physical sizes of the sources in the MS.

6.2.2 Size considerations

We measured the largest angular size (LAS) at *C* band (~ 4.8 GHz) of each source in the MS using VLA *C*-array band imaging for the northern sources and ATCA 6-km for the southern sources. There is a small bias here in that the VLA-*C* is slightly more sensitive to resolving larger scale structures. Sizes were extracted using the AIPS task TVDIST for resolved sources or alternatively, the major-axis of the Gaussian beam as fit by the AIPS task JMFIT was taken as an upper limit on the LAS for unresolved sources. Angular sizes were converted to physical scales using the Interactive Data Language (IDL) routine, ZANG. In Fig. 11 we replot the bottom panel of Fig. 10 but now weight the symbol size by the physical size of the non-core that it represents (LAS in kpc scaled by constant but arbitrary factor). We do not include here the MS+ extension sources, in order to keep as much consistency as possible in the array configurations from which our LASs were measured. However, we note that archival images of the sources in the MS+ extension show similar size distributions to those observed in the MS.

The most powerful non-cores at any given X-ray luminosity – those sources found above the dotted line in Fig. 11 – are typically large resolved sources. Specifically, in order of increasing cluster X-ray luminosity these sources are A2634, RX J2214.7+1350, A160, RX J0058.9+2657, A407, A3581, Z1261, RX J1320.1+3508, A2627a, A2055 and A1763. All of these except A3581 are large jetted systems, of which A2627a shows one sided jetted structure and all others show classical FRI/II type morphology. A3581 has only a hint of a resolved jet with ATCA-6-km *C*-band observations. Canning et al. 2013 however use the hybrid VLA-AnB array at *L* band to show this source has radio lobes that fill the X-ray cavities in this system. The small extent and currently highly active core

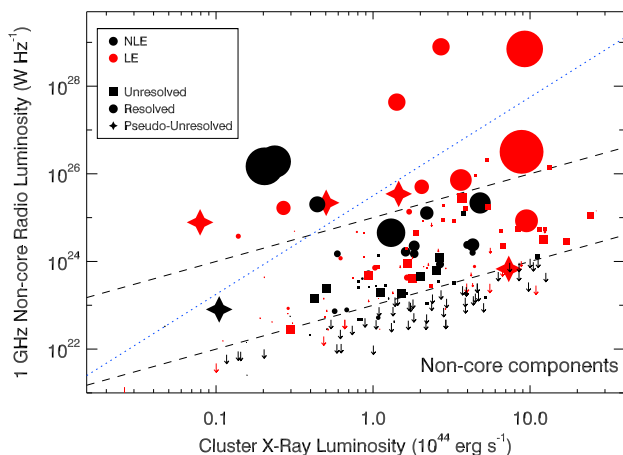


Figure 11. As for bottom panel of Fig. 10 except only for the MS and now symbols are sized by physical size of the non-core component, as seen at *C* band with either the VLA *C* array or ATCA. Note that stars represent sources where extended emission is resolved out at this resolution but where lower resolution and/or lower frequency observations show distinctive lobed features – i.e. they are resolved out with our sampling but there is known extended emission in the systems, so they are effectively ‘pseudo-unresolved’. Colours again represent the state of the cluster (black NLEs, red LEs) although circles now show sources that are resolved (at this resolution) and squares those that are unresolved and hence represent upper limits. Sizes were measured as LAS. For unresolved sources, the major axis of the beam was taken as the size limit. The dashed lines are illustrative only and represent one-to-one normalization with a two order of magnitude separation. The dotted line represents a normalization power law of order three and is used only as a differentiator (see text). [A colour version of this figure is available in the on-line journal.]

suggests the non-core emission here is recently injected and may perhaps be expected to expand outwards in future, which could classify this source as a young FRI/II precursor. That the majority of the most powerful non-cores at any given X-ray luminosity are large FRI/II type sources supports the idea that powerful individual periods of activity may be responsible for the brightest non-cores and that in a larger sample we may expect to find bright cores in low X-ray luminosity clusters.

However, the general distribution shown by the bulk of the population below the dotted line in Fig. 11 is comprised of a mixture of large extended resolved and smaller unresolved sources over the full range of X-ray luminosities. The extended sources here represent a mixture of FR type and more amorphous sources. That there is a general trend for brighter non-cores to reside in more X-ray luminous clusters regardless of their size but that the brightest tend to all be large extended sources suggests there may be two different activity types occurring in BCGs.

Continuous (or repeated) core activity may lead to confused, fairly amorphous small-scale structures comprised of accumulated material from extended periods of core activity. The tendency for more powerful cores to inhabit more X-ray luminous clusters would then naturally account for brighter non-cores inhabiting these same clusters. However, any BCG (indeed, any AGN) can experience a single strong outburst, powerful enough to eject material well beyond the immediate BCG vicinity and manifest as a lobe-dominated FR-type source, potentially explaining the powerful non-cores in less X-ray luminous clusters.

The overall brightness of the non-core will thus be a superposition of the accumulated material and the single powerful outburst, which could explain the extremely bright emission for the most-powerful non-cores in X-ray luminous clusters – if they are powerful FR-type non-cores superposed on top of a pedestal of accumulated emission.

In between large outbursts, the AGN remains persistently active albeit at a lower radio power, which is reflected in the high portion of (especially) LE BCGs that have an active core component. This suggests that when studying AGN it is important not only to look at the time a source is radio-loud for, but also the fraction of this time for which the AGN is actively launching jets.

6.3 [O III] 5007 Å correlations

To investigate the relationship of radio emission to other tracers of AGN activity, we consider the high ionization [O III] 5007 Å forbidden line, which can be used as a canonical tracer of current AGN activity (Maiolino & Rieke 1995). Combining long slit observations taken with the New Technology Telescope (NTT) and Very Large Telescope (VLT; Edge et al., in preparation) with those in Crawford et al. 1999, we have [O III] fluxes for 97 of the sources within our MS+ (of which 13 are in the MS+ extension).

These [O III] fluxes are all from long slit observations of 1.2–1.5 arcsec width so there will be some flux lost outside the slit. However, on the whole the nuclear [O III] emission will dominate over the more extended, non-AGN emission so these fluxes should be representative of any underlying correlation. Four of these sources (A2146, A1068, RX J0821.0+0752, Z3146) are believed to host strong Type II AGN as a result of high MIR fluxes, high [O III]/H β ratios and very red 4.5/3.6 μ m colours (Egami et al. 2006; O’Dea et al. 2008; Quillen et al. 2008). The presence of this strong MIR-AGN component will boost the [O III] fluxes within these objects above our typical sample and hence they do not represent a fair comparison. We therefore highlight these objects in Fig. 12 and remove them from the subsequent fits.

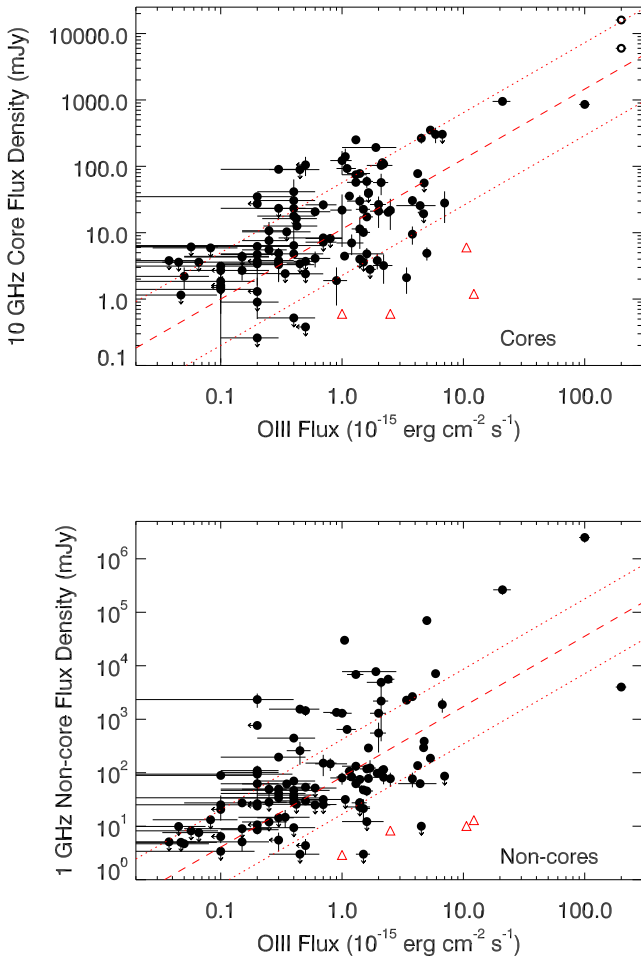


Figure 12. The 10 and 1 GHz normalized, respectively, core and non-core radio flux components plotted against the [O III] $\lambda 5007 \text{ \AA}$ flux. The dashed line in the top panel marks a linear correlation between the [O III] 5007 \AA and core radio flux which spans four orders of magnitude in each parameter (see Section 6.3). The dotted lines mark a factor of 20 in scatter either side of the relation. A correlation is also found for the non-core (bottom panel), although with significantly increased scatter, as highlighted by the inclusion of the dotted lines again indicating a factor of 20 scatter in either direction. Red triangles are sources significantly contaminated by a mid-infrared (MIR)-dominated AGN and are not included in the fit (see text). NGC 1275 is shown twice in the upper panel (open circles) to highlight the variability of its core over \sim decade time-scales. Such variation in the sample as a whole is expected to account for a significant portion of the scatter. [A colour version of this figure is available in the on-line journal.]

To increase our coverage, we identify an additional 16 systems for which equivalent [O III] measurements are available that do not fall within our parent sample yet have comparable properties and hence are included within this analysis. For each of these additional 16 sources, we populate their radio SEDs from the literature and perform decompositions (see Section 4 and Table F1). This creates a total [O III] sample of 113 BCGs.

Using the `BHKMETHOD` tool within the Image Reduction and Analysis Facility (`IRAF`) shows that [O III] flux is correlated with *both* the core and non-core radio flux. Both return a probability of no correlation < 0.001 (the limit) with calculated Kendall’s τ coefficients of 0.7533 and 0.7272, respectively. We use the `BUCKLEYJAMES` linear regression tool within `IRAF` to compute best fits to the data. This algorithm can handle censors only in the dependent variable of a

data set. Neither of our variables is truly independent. We assign the [O III] line flux as our independent variable, since we have selected this subsample on the availability of [O III] data and also it requires the smallest removal of data. Nine sources with [O III] limits are removed. The recalculated Kendall’s τ coefficients are 0.7661 and 0.7508 for the cores and non-cores, respectively, so the removal has a minimal effect.

Between the [O III] (in $\text{erg cm}^{-2} \text{ s}^{-1}$) and core radio (mJy at 10 GHz) fluxes we find a best-fitting power law:

$$\log_{10}(S_{\text{Core}}) = (1.05 \pm 0.10) \log_{10}(F_{\text{OIII}}) + (1.05 \pm 0.01). \quad (5)$$

The equivalent correlation between [O III] and the non-core radio component (normalized at 1 GHz) is

$$\log_{10}(S_{\text{NC}}) = (1.31 \pm 0.16) \log_{10}(F_{\text{OIII}}) + (1.92 \pm 0.06). \quad (6)$$

Although it appears in Fig. 12 that the correlations are driven largely by the bright local sources NGC 1275, M87 and Cygnus A, if these sources are removed then `IRAF` returns consistent fits, still with a probability of no correlation < 0.001 . We therefore conclude that the presence of these correlations is robust.

6.3.1 [O III] discussion

The correlations between the radio component’s flux and [O III] flux (see Fig. 12) support previously found correlations between radio and [O III] luminosities (e.g. Rawlings et al. 1989 at 178 MHz; de Vries et al. 2007 at 1.4 GHz; Tadhunter et al. 1998 at 2.7–5 GHz). Interestingly, Rawlings et al. found a correlation between the [O III] and total radio power but only low-significance indication for a correlation between the resolved ‘core’ radio and the [O III] in their sample. Here we see such a correlation, with reduced scatter over that of the more extended emission.

Our results show that whilst both radio components correlate with the [O III], there is less scatter when considering only the radio core component (see Fig. 12). Along with a loose intrinsic link between core and non-core power (see also Section 6), this suggests that the primary correlation is with the core component. There is tentative evidence ($< 2\sigma$) that the index for the correlation with the non-core component is steeper than for the core component. We interpret this as evidence for the core component driving the correlation, as the [O III] forbidden line is collisionally de-excited and so traces recent AGN *core* activity. Conversely, if the non-core emission is due to the cumulative effect of long-term activity then it should show more radio emission for a given [O III] flux.

Labiano 2009 found a correlation between the [O III] and 5 GHz radio power that had increasing gradient when considering only GPS, GPS+compact steep spectrum (CSS), only CSS and then combined GPS+CSS+FR-type radio sources. Assuming the commonly quoted interpretation of these source types as a loose evolutionary sequence, GPS sources are expected to be core dominated whereas the large, extended FR-type sources are most likely to be dominated by their extended emission at 5 GHz. Indeed, the sources with the highest $F_{\text{NC}}/[\text{O III}]$ flux ratios in the bottom panel of Fig. 12 correspond to the most physically extended sources (as seen in Fig. 11). Under such assumptions this then supports our interpretation that the correlation is core driven. It follows that a significant portion of the scatter found in relations between radioactivity and AGN activity at other wavelengths is due to the varying time-scales on which the emission was produced.

6.4 Cavity correlations

6.4.1 Insight into the activity cycle

For statistically relevant samples, BCG radio power correlates well with the cavity power, albeit with large scatter (e.g. Birzan, Rafferty & McNamara 2004; Birzan et al. 2008; Cavagnolo et al. 2010). These studies usually depend upon the total radio power at L band. Here we attempt to expand upon this by considering how the cavity power correlates with both the core and non-core radio powers. A literature search for X-ray cavity systems amongst our MS was performed, and supplemented by recently discovered cavity systems (Hlavacek-Larrondo, private communication). 26 of our MS clusters have known X-ray cavities, of which 23 are LEs, with the remaining three (A189, RX J0419.6+0225 and RX J1522.0+0741) being weak cavity systems in low-redshift clusters.

Cavity powers are estimated using the standard techniques (e.g. Birzan et al. 2004). The total enthalpy is given by $4pV$, where p is the thermal pressure at the radius of the bubble measured from X-ray observations and V is the volume of the cavity. We assume that the cavities are of prolate shape: $V = 4\pi R_w R_l/3$, where R_l is the projected semimajor axis along the direction of the jet and R_w is the projected semimajor axis perpendicular to the direction of the jet. Errors on the radii are assumed to be ± 20 per cent. Cavity powers are then calculated by dividing the enthalpy with the buoyancy rise time of the cavity (Churazov et al. 2001). The latter measures the time it takes a cavity to reach its terminal buoyancy velocity.

Fig. 13 shows the cavity power both as a function of the non-core and core radio components (top and middle panels, respectively). Using the IRAF BHKMETHOD tool for linear regression, we encouragingly find that the cavity powers strongly correlate with the non-core radio powers (Kendall's $\tau = 0.9538$, with probability of no correlation 0.02 per cent). This correlation is expected, since non-core emission is usually composed of dying radio emission in lobes that are cospatial with cavities and hence commonly traces the same outburst as that which evacuated them.

There is also a reasonably secure correlation (Kendall's $\tau = 0.5723$, with probability of no correlation < 1 per cent) between the cavity power and the core radio component. This is more surprising, as the bubble-rise time-scale should be long enough to decouple the cavity power from what is happening in the core unless the core activity is persistent over time-scales of several Myr. This is therefore indicative of steady AGN fuelling in BCGs over bubble-rise time-scales.

Regression fits to the data are performed using the IRAF BUCKLEYJAMES algorithm. As in Section 6.3 neither of our variables is truly independent. We assign the cavity power as the independent variable for fitting purposes since this subsample was selected on the basis of having observed cavities. However, note that in Fig. 13 we plot cavity power as the ordinate to ease comparison with earlier studies. We find best-fitting power laws

$$\log_{10}(P_{\text{NC}}) = (1.022 \pm 0.18) \log_{10}(P_{\text{Cav}}) + (24.03 \pm 0.16) \quad (7)$$

for the non-core component and

$$\log_{10}(P_{\text{Core}}) = (0.86 \pm 0.36) \log_{10}(P_{\text{Cav}}) + (22.80 \pm 0.27) \quad (8)$$

for the core component, respectively. Note that a fit to the integrated L -band power gives a consistent result with the fit to the non-core power, as should be expected since the non-core tends to dominate at this frequency.

We further consider the non-core to cavity power correlation, splitting the non-core radio component into those with the steepest

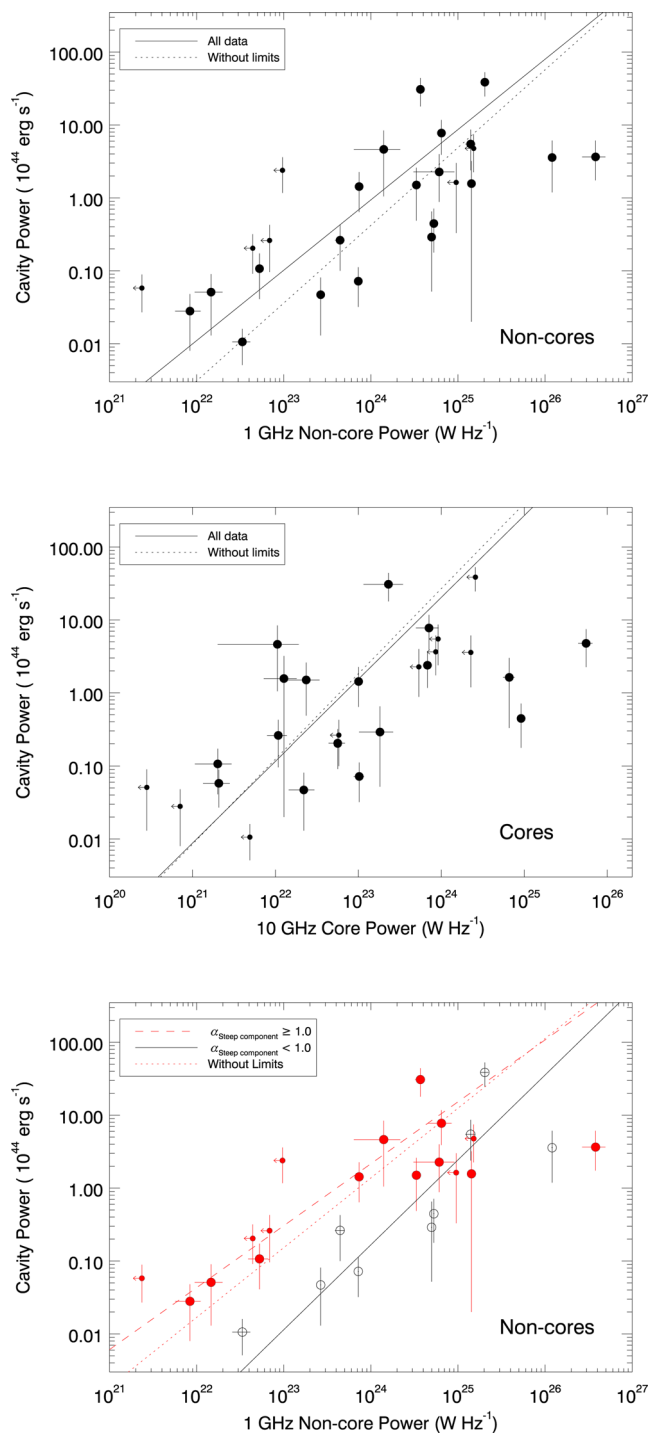


Figure 13. Correlations between both the non-core radio luminosity and cavity power (top) and core radio luminosity and cavity power (middle). Solid lines are the regression fits to the full data sets, as found using the BUCKLEYJAMES algorithm within IRAF, and dotted lines are linear fits when the upper limits on the radio data are neglected. A correlation with the non-core emission is expected whereas the one with the core is less expected, suggesting that central AGN activity is persistent on bubble-inflation/rise time-scales. Also shown is the non-core to cavity power relationship divided on the radio spectral index of the steep component (bottom). Filled circles have $\alpha_{\text{steep component}} \geq 1.0$ whereas open circles have $\alpha_{\text{steep component}} < 1.0$. A clear index-dependent split is seen. See text for implications. [A colour version of this figure is available in the on-line journal.]

spectral indices $\alpha \geq 1.0$ and those with flatter indices $\alpha < 1.0$ (see Fig. 13, bottom panel). This value is chosen so as to include the limits as steeper spectrum objects, which is reasonable for these clusters as they tend to be well sampled in the GHz range and flatter components would be expected to be detected. A separation is seen in the lower panel of Fig. 13. For a given cavity power, steeper spectrum non-core components tend to be lower power than flatter spectrum non-cores. Note that the apparent steep spectrum outlier lies in a system (Abell 115) with a prominent extended radio relic (Govoni et al. 2001), which may be contaminating and inflating the non-core flux measurement. If limits are removed from this bottom panel, then such a split is still observed. We propose that this apparent split is suggestive of evolution of the radio emission within individual cavities.

The regression fits return best-fitting power laws to our split data of

$$\log_{10}(P_{\text{NC}}) = (0.86 \pm 0.18) \log_{10}(P_{\text{cav}}) + (24.67 \pm 0.03) \quad (9)$$

for when the non-core component has index $\alpha < 1.0$ and

$$\log_{10}(P_{\text{NC}}) = (1.22 \pm 0.21) \log_{10}(P_{\text{cav}}) + (23.51 \pm 0.03) \quad (10)$$

for when the non-core component has index $\alpha \geq 1.0$, respectively.

When cavity inflation ceases and the inflated cavity detaches from the BCG, its power is virtually fixed. Increasing volume of the cavity as it propagates is counteracted by the lowering of the surrounding pressure. However, the synchrotron emitting electron population within the cavity will begin to age, hence the radio spectrum will steepen over time. This will contribute significant scatter within the radio power to jet power ratio. Isolating the non-core radio emission and including the low-frequency radio spectral index of this as an additional parameter in such studies could potentially eliminate much of the scatter.

7 DISCUSSION

That BCGs exhibit increased likelihood of hosting radio-loud AGN is well established (e.g. Burns 1990; Best et al. 2005). The trends presented above explore beyond this, showing that there is a great range of behaviour beyond generic ‘radio-loudness’ that appears to be driven largely by environment.

7.1 LE to NLE differences

Striking differences are seen in both the frequency of radio-loudness and in the resulting radio luminosity of the AGN between those in LEs and those in NLEs. Considering Fig. 4 we see that ~ 50 per cent of LE-BCGs host AGN with radio powers above $10^{24} \text{ W Hz}^{-1}$ at L band as opposed to only ~ 15 per cent equivalent for NLEs. Our overall detection fractions for radio-loudness at L band are equivalent to those of other X-ray selected cluster samples. However, they are above those for otherwise detected samples (see Section 5.2). When we remove LE-BCGs from the sample we recover a detection fraction similar to that of otherwise selected massive galaxies (Best et al. 2005). This suggests that the AGN activity of NCC-hosted BCGs is largely governed by the same processes as isolated galaxies of similar mass. That is they are affected mainly by their own circumgalactic envelopes. That the detection fraction for LE BCGs jumps significantly above this shows unequivocally that the cooling flow must be causing the increased duty cycle of radio-loudness, therefore, it seems natural that this same cooling is, directly or indirectly, fuelling the AGN.

7.1.1 Decomposed luminosity functions

We plot in the top and middle panel of Fig. 14, separate luminosity functions for the core and non-core components, considering only sources in the MS. In the bottom panel of Fig. 14 we show the equivalent plot to Fig. 4 but incorporating only the sources in the MS. We see that the total split at L band is driven by the non-cores, as expected since this is the component that tends to be most dominant at ~ 1 GHz and is usually brightest overall. However, we see that the LE to NLE dichotomy is enhanced when considering only the cores. Core components in LEs are typically two orders of magnitude more powerful than those in NLEs. This split is equivalently shown in Fig. 15, where limits are conservative. Error bars show the range of the maximum and minimum separations of the distributions in Fig. 14 if all cores lay infinitely or infinitesimally below the limits.

In Fig. 16 we show the equivalent plot to Fig. 14 but now include the full MS+. Again, a larger split is seen for the core components.

7.2 Dual-mode feedback – a duty cycle within a duty cycle

Whilst LE-BCGs have a higher duty cycle of radio-loudness than NLEs, what is really striking is that the fraction of radio-loud sources that contain an *active* core component is also much higher in LEs. In effect this is an *inner duty cycle* – the portion of radio-loud time for which an AGN is actively injecting radio emitting populations – and it appears to be this factor that really characterizes the difference between LEs and NLEs.

Several studies have shown that direct Bondi accretion of the hot gas on scales < 1 kpc from the nucleus can provide adequate fuel *on average* (see McNamara & Nulsen 2007). This rate is however too low for the most extreme outbursts (e.g. McNamara, Rohanizadegan & Nulsen 2011). Allen et al. 2006 claim a strong correlation between the Bondi rate and their measured cavity powers in a small sample of well-observed, local systems. However, Russell et al. 2013 find a much weaker relationship.

In their recent review Heckman & Best 2014 argue that a plausible explanation for these disparate results may be that Bondi accreting gas goes through an intermediate stage where it cools prior to finally being accreted on to the black hole. Alternatively, the AGN may be fuelled by cold phase accretion whereby blobs of cold gas condense non-linearly at scales $\sim 5\text{--}30$ kpc from the black hole and infall on less than the cooling time-scale (e.g. Pizzolato & Soker 2005). In a recent paper considering the origin of multiphase gas in CCs, Voit & Donahue (2015) find that thermal conduction and cold-mode accretion are complementary processes in regulating cluster cores. At higher core entropies conduction prevents the core from cooling radiatively whereas at lower entropy, thermal instabilities cause the formation of cold clouds that subsequently precipitate on to the central black hole and power AGN feedback. These scenarios all require that in some systems there should be large amounts of cold gas near to the nucleus. Indeed there is evidence for rotating discs of cool gas in some BCGs (e.g. Simkin 1979; Ekers & Simkin 1983; Lim et al. 2000; Wilman, Edge & Johnstone 2005; Hamer et al. 2014; Russell et al. 2014). The resultant cold clouds could then power the sporadic periods of high activity whilst the AGN activity could still relate to the wider Bondi rate *on average*.

Such a scenario appears likely within cluster cores, where the cooling flow deposits large amounts of molecular gas within the BCG. The steady build-up of such cold clouds ensures that the replenishment time is low and hence naturally explains the high duty cycle of radio-loudness in both NLEs and LEs. The high *inner duty cycle* of *active* core components in LEs is slightly trickier to

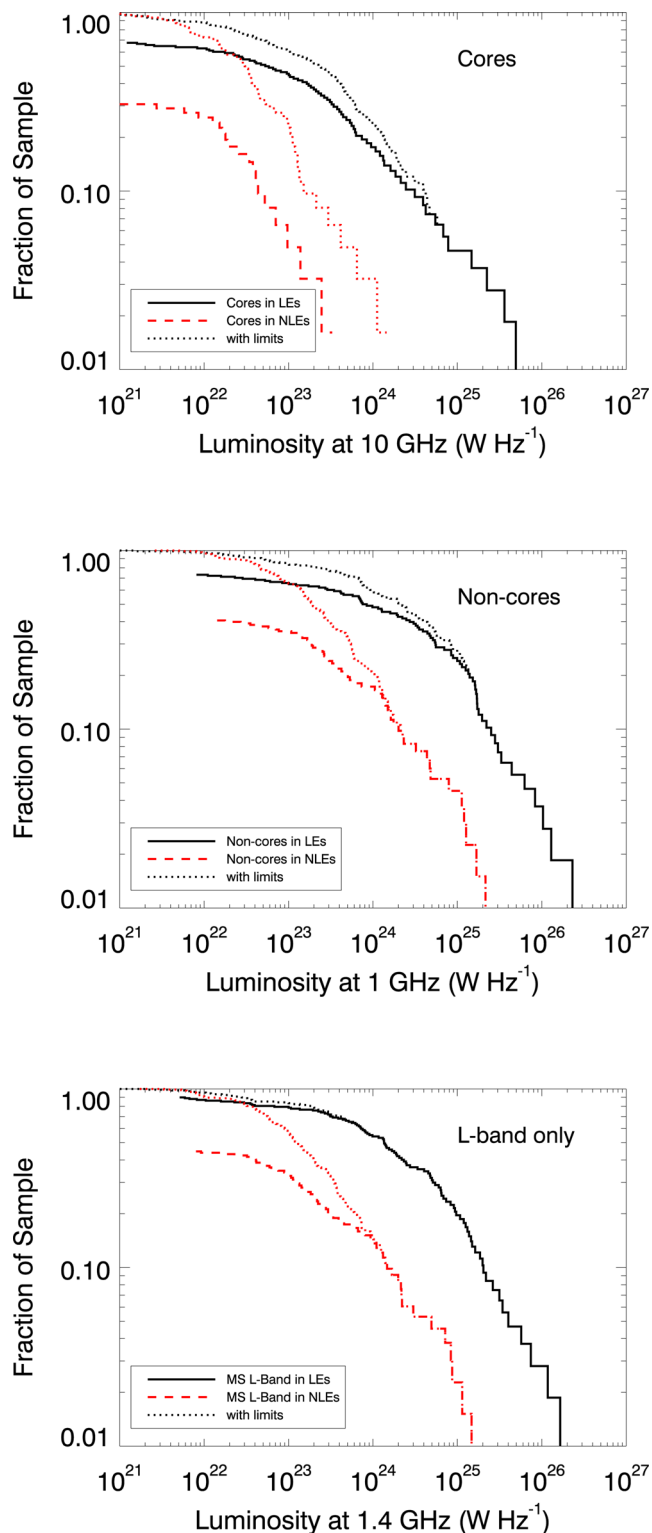


Figure 14. As for Fig. 4 but now using only the core components at 10 GHz (top), the non-core components at 1 GHz (middle) and the 1.4 GHz monochromatic flux for only those sources in the MS. Note that the overall spectrum at 1.4 GHz is most often dominated by non-core emission, as is reflected in the similarity between the split at L band and that of the non-core component. However, the core activity is apparently even more environmentally dependent, with core powers in NLEs typically being up to two orders of magnitude less than those in LEs. [A colour version of this figure is available in the on-line journal.]

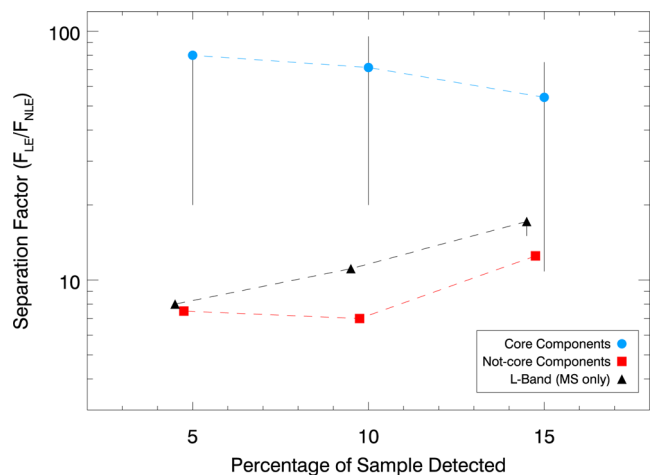


Figure 15. Separation of the LF distributions for LEs and NLEs in terms of the ratio of their detection fraction, for the core components, non-core components and the equivalent 1.4 GHz monochromatic LF for only those sources in the MS, as shown in Fig. 14. Error bars are the maximum and minimum separation possible accounting for limits and hence are not truly ‘errors’. The large lower uncertainties on the cores shown here are expected to be hugely overestimated by this method as it would require all sources with a core limit to have an active core so far overlooked from observation, which we deem highly improbable. Considering this, a clear difference in core activity as a function of cluster environment is claimed. Note that X-positions have been shifted slightly for clarity. [A colour version of this figure is available in the on-line journal.]

comprehend purely by sporadic processes. We postulate that within the LE clusters both ready cooled material and direct hot phase gas fuel the AGN. The clumpy cold clouds would be responsible for the brighter periods of activity (Werner et al. 2014). In between these periods, a steady trickle of hot gas would still be able to reach the nucleus ensuring the persistency of core emission. It could be that the presence of a weak Bondi-powered jet catalyses the formation of cold clouds that can then fuel more powerful activity.

This behaviour closely agrees with models of chaotic cold accretion (e.g. Gaspari, Brighenti & Temi 2015) where under idealized conditions, cool clumps condense from the ICM due partly to the actions of jetted outflows. Cold accretion of these jet-induced clumps then boosts the accretion to well above ($\sim 100x$) the Bondi rate (Gaspari, Ruszkowski & Sharma 2012), whereas purely hot-mode accretion dominates during the quiescent periods in between (see also Li & Bryan 2014). Such a process may be partly responsible for the so-called ‘molecular fountains’ seen in some BCGs (e.g. A1835; McNamara et al. 2014) where cool material appears to condense behind rising cavities before falling back towards the central engine.

7.2.1 Accretion mode considerations

We have not in this paper explicitly classified our BCGs as low-excitation or high-excitation radio galaxies (LERGs or HERGs, respectively), a distinction that appears strongly related to the accretion state (inefficient/efficient, respectively, for LERGs/HERGs; Best & Heckman 2012). However, the vast majority of BCGs are LERGs, typified by accretion efficiencies $L < 0.01 L_{Edd}$ (where L_{Edd} is the Eddington luminosity). At these low rates, accretion is believed to be via an advection-dominated accretion flow (ADAF). Whatever the coupling efficiency of the mechanical energy output by a BCG, this is not likely to substantially change over the

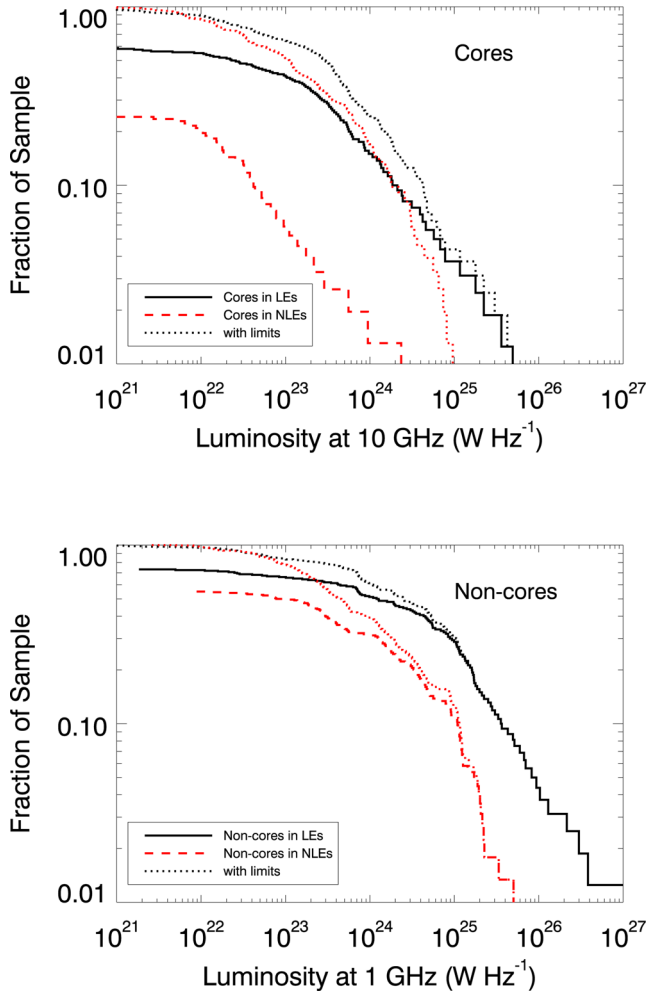


Figure 16. As for Fig. 14 but using the MS+. Note that unlike the MS, which was largely unbiased on radio priors (see Section 2.2), the MS+ extension is flux limited at L -band radio and hence contains a smaller fraction of radio-quiet objects than is truly representative of the full parent sample. The LF extrema given when limits are included are hence essentially useless for inference purposes and stand only to highlight our ignorance of the full picture when limited data are available. Notwithstanding, we see here that the larger split is seen amongst the core values (it stands to reason that all cores should be detected within the radio-loud rather than radio-quiet sample!). The smaller split in non-cores (as compared to Fig. 14) can be attributed to this bias, since with the plot being cumulative the relatively lower detection amongst NLEs in the parent sample would serve to separate the lines further. That the core split remains large amongst the entirety of the radio-loud BCG sample (to given limit) further strengthens the case that this is a genuine example of the environment affecting AGN behaviour in a systematic way throughout the Universe. [A colour version of this figure is available in the on-line journal.]

range of luminosities we see in our sample as they always remain in the LERG, ADAF stage. Changes in radio luminosity are therefore most likely to correspond to changes in mechanical feedback power (as corroborated by Fig. 13), rather than large changes in the accretion structure such as the collapse of an ADAF into a classical Shakura–Sunyaev thin disc (e.g. see review of accretion structures by Done, Gierlinski & Kubota 2007).

Additionally, in analogy with the scenario seen in black hole binaries, the transition from an ADAF to a thin-disc accretion mode may be expected to coincide with a switch from magnetically ar-

rested to magnetorotationally supported accretion and hence the launching of a short-term ballistic jet (Mirabel & Rodríguez 1994; Remillard & McClintock 2006; Dexter et al. 2014). Such an event would cause the collapse of the large scale-height magnetic fields present in the inner accretion zone that are required for the launching of a typical steady jet (e.g. Mirabel et al. 1992; Fender 2001). The apparently highly persistent activity we infer from our sample would oppose such a magnetic restructuring, certainly for our LEs. That the periods of higher activity correspond to a difference in accretion structure (namely, a transition to a thin disc) are therefore considered highly unlikely and instead more likely correspond to something more akin to a greatly scaled-up analogue of the flaring seen in Sgr A*.

7.3 Considering relativistic beaming

For the size of our parent sample, geometry causes us to expect ~ 20 sources to be aligned within $\sim 5^\circ$ of the line-of-sight. Such a population may present itself as a population of flat spectrum, apparently powerful cores but would have their intrinsic core powers overestimated by potentially large factors. However, note that we purposefully removed BLLac objects from our parent sample so as not to be overtly affected by a handful of strongly beamed sources. There is also no logical reason why LE-BCGs would more commonly have aligned cores than NLEs.

Relativistic beaming of the inner jet in an existing radio source could account for some seemingly strong, flat spectrum components of otherwise steep spectrum sources if the jet axis has precessed into favourable alignment. Our sample does include a couple of sources that have previously been considered to be mildly beamed. For example, the BCG of A2055 appears to be a head–tail source on few arcsecond scales, but the bright core may be beamed (Pimblet et al. 2006). Similarly, A2627a only appears to have marginally resolved jet structure on arcsecond scales but its AGN is X-ray dominated, hence the flux may be boosted by the presence of a beamed BLLac-like nucleus (Rector, Stocke & Perlman 1999). However, for this to account for all our split spectrum sources would require a very high precession speed in a significant number of sources. Additionally, the long time-scales between some of the archival data we use in compiling our SEDs show that the flat and GPS-like behaviour is persistent over more than decade time-scales. This is therefore unlikely to be purely the result of beaming, which would give significant, short-term variation. Furthermore, VLBA imaging of the central regions shows symmetrical two-sided structures on few parsec scales in many of our active BCGs hence showing that the source is not favourably aligned for strong beaming. This VLBA data will be presented in an upcoming paper.

Overall, we concede that some blurring of results due to relativistic effects are essentially unavoidable for any large sample of radio AGN, however, due to the arguments stated here we do not believe beaming to overtly affect our results.

7.4 Survey considerations and mimicked evolution

The presence of two very different radio components in the SEDs of BCGs, means that the source population sampled in a flux-limited radio survey of AGN is highly dependent upon the observed frequency; unlike the case for a population of single spectral index sources. Higher frequency samples (roughly comparable to a horizontal split on Fig. 8) will contain a higher proportion of core-dominated systems whereas low-frequency selected samples (more

equivalent to a vertical split in Fig. 8; Tingay et al. 2013; van Haarlem et al. 2013) will favour those dominated by steeper spectrum emission (see also Sadler et al. 2014). Whilst it is already well established that high-frequency surveys will preferentially detect young sources, for BCGs the effect is slightly more subtle in that high-frequency samples will preferentially detect those sources with the highest *inner duty cycle* of core activity (i.e. BCGs that are more persistent).

As the youngest and most recent AGN activity will peak spectrally at higher frequencies (e.g. O’Dea 1998; Sadler et al. 2014), samples taken at frequencies below the characteristic turnover will preferentially detect older outbursts. Samples at progressively higher frequencies will therefore contain a greater proportion of younger sources. Conversely, for a single observing frequency, matching samples at increasing redshift will show the same effect such that the population of radio sources to higher redshift, particularly for redshifts greater than 2 (where a rest frame ~ 15 GHz characteristic GPS peak would be redshifted below 5 GHz), will appear younger and more active – effectively mimicking evolution in the source population.

Much increased spectral coverage is required before improvements to the radio *k*-correction above a simple power-law extrapolation will be confirmed possible/necessary or not. However, the effect should be considered when studying the redshift evolution of the radio population.

The powerful core components in LE-BCGs, especially in instances where these cause spectral peaks to higher radio frequencies, may be an important contaminant in Sunyaev–Zel’dovich (SZ) cluster surveys. The ramifications of these strong core components are explored in a sister paper, Hogan et al. (2015).

8 CONCLUSIONS

We have studied the radio properties of BCGs drawn from a large sample of X-ray selected galaxy clusters. The sample is split by the presence of optical emission lines ($H\alpha + [N II]$), using the proxy that when these lines are present the cluster most likely corresponds to being a strong CC and when absent the dynamical state of the cluster is markedly less relaxed. We present and collate a large radio data volume for this sample and consider the overall radio properties of the sample as a function of environment. Furthermore, we decompose the BCG radio emission into two components – a core, attributable to ongoing injection AGN activity, and a non-core, comprising everything else. We then consider these components in order to better understand the activity. Chiefly we find the following.

(i) The duty cycle of radio-loudness is significantly higher for BCGs in strong CC clusters (>85 per cent) than for those in non-strong CC clusters (>52.5 per cent).

(ii) LE BCGs are typically much more radio powerful AGN than those in NLEs – ~ 50 per cent of LE BCGs hosting a radio source $> 10^{24}$ W Hz $^{-1}$ at 1.4 GHz whereas only ~ 15 per cent are similarly radio powerful in NLEs.

(iii) The prevalence, and typical power, of an *active* radio core is highly dependent on cluster state. 60.2 per cent of LE BCGs in our sample contain a distinguishable core of which ~ 83.1 per cent are $> 10^{23}$ W Hz $^{-1}$. Conversely, only 11.6 per cent of our NLE BCGs contain a distinguishable core, with only ~ 5.0 per cent of our NLE BCGs containing an active core of $> 10^{23}$ W Hz $^{-1}$.

(iv) This core component shows better correlation with the canonical AGN tracer, $[O III] 5007 \text{ \AA}$, than the ageing non-core

component. It is thus likely that significant scatter often found in studies between radio emission (particularly from low-resolution surveys) and other AGN tracers is due to long time lapses between emission periods.

(v) The brightest cores are only hosted by the most X-ray luminous clusters, although bright non-cores can be hosted by both high and low X-ray luminosity clusters.

(vi) Both non-core and core radio emission correlate with cavity power in LEs. It appears that BCGs are persistently radio active over bubble-rise time-scales in these environments.

(vii) The radio power versus cavity power correlation appears to evolve with the spectral index of the radio source.

(viii) An increasing fraction of flat and inverted spectrum sources in samples selected at increasing radio frequency may mimic luminosity evolution in the total radio population if not fully accounted for.

Overall, we find that BCGs are a varied population with a wide variety of radio behaviour. Future studies in the so-called ‘new golden age’ of radio astronomy that we are now entering with existing and upcoming facilities should uncover many more facets to these intriguing behemoths.

ACKNOWLEDGEMENTS

We thank the anonymous referee for useful comments and suggestions that have greatly improved this work. MTH acknowledges support from the Science and Technologies Funding Council (STFC), studentship number ST/I505656/1. ACE acknowledges support from STFC grant ST/I001573/1. ACF and HRR acknowledge support from ERC Advanced Grant Feedback. HRR also acknowledges support from a COFUND Junior Research Fellowship at the Durham University Institute of Advanced Study. This research has made use of the NASA/IPAC Extragalactic Database (NED) which is operated by the Jet Propulsion Laboratory, California Institute of Technology, under contract with the National Aeronautics and Space Administration. This research has made use of data, software and/or web tools obtained from NASA’s High Energy Astrophysics Science Archive Research Center (HEASARC), a service of Goddard Space Flight Center and the Smithsonian Astrophysical Observatory. This research used data from the NRAO archive. The National Radio Astronomy Observatory is a facility of the National Science Foundation operated under cooperative agreement by Associated Universities, Inc. This research work has used the TIFR GMRT Sky Survey (<http://tgss.nrao.tifr.res.in>) data products.

REFERENCES

- Allen S. W., Dunn R. J. H., Fabian A. C., Taylor G. B., Reynolds C. S., 2006, *MNRAS*, 372, 21
 Araya E. D., Rodriguez C., Pihlstrom Y., Taylor G. B., Tremblay S., Vermeulen R. C., 2010, *AJ*, 139, 17
 Augusto P., Edge A. C., Chandler C. J., 2006, *MNRAS*, 367, 366
 Baars J. W. M., Genzel R., Pauliny-Toth I. I. K., Witzel A., 1977, *A&A*, 61, 99
 Becker R. H., White R. L., Helfand D. J., 1995, *ApJ*, 450, 559
 Belsole E., Birkinshaw M., Worrall D. M., 2005, *MNRAS*, 358, 120
 Benson A. J., Bower R. G., Frenk C. S., Lacey C. G., Baugh C. M., Cole S., 2003, *ApJ*, 599, 38
 Best P. M., Heckman T. M., 2012, *MNRAS*, 421, 1569
 Best P. N., Kauffmann G., Heckman T. M., Brinchmann J., Charlot S., Ivezić Z., White S. D. M., 2005, *MNRAS*, 362, 25

- Best P., von der Linden A., Kauffmann G., Heckman T. M., Kaiser C. R., 2007, *MNRAS*, 379, 894
- Birzan L., Rafferty D. A., McNamara B. R., 2004, *ApJ*, 607, 800
- Birzan L., McNamara B. R., Nulsen P. E. J., Carilli C. L., Wise M. W., 2008, *ApJ*, 689, 859
- Blanton E. L., Sarazin C. L., McNamara B. R., Wise M. W., 2001, *ApJ*, 558, L15
- Böhringer H. et al., 2004, *A&A*, 425, 367
- Bourda G., Charlot P., Porcas R. W., Garrington S. T., 2010, *A&A*, 520, A113
- Bourda G., Collioud A., Charlot P., Porcas R., Garrington S., 2011, *A&A*, 526, A102
- Bower R. G., Benson A. J., Malbon R., Helly J. C., Frenk C. S., Baugh C. M., Cole S., Lacey C. G., 2006, *MNRAS*, 370, 645
- Brough S., Collins C. A., Burke D. J., Mann R. G., Lynam P. D., 2002, *MNRAS*, 329, L53
- Brunetti G., Jones T. W., 2014, *Int. J. Modern Phys. D*, 23, 1430007
- Burns J. O., 1990, *AJ*, 99, 14
- Burns J. O., Sulkanen M. E., Gisler G. R., Perley R. A., 1992, *ApJ*, 388, L49
- Canning R. E. A. et al., 2013, *MNRAS*, 435, 1108
- Carlstrom J. E. et al., 2011, *PASP*, 123, 568
- Cavagnolo K. W., Donahue M., Voit M., Sun M., 2008, *ApJ*, 683, L107
- Cavagnolo K. W., McNamara B. R., Nulsen P. E. J., Carilli C. L., Jones C., Birzan L., 2010, *ApJ*, 720, 1066
- Churazov E., Brügggen M., Kaiser C. R., Böhringer H., Forman W., 2001, *ApJ*, 554, 261
- Churazov E., Ruszkowski M., Schekochihin A., 2013, *MNRAS*, 436, 526
- Cleary K. A. et al., 2005, *MNRAS*, 360, 340
- Coble K. et al., 2007, *AJ*, 134, 897
- Cohen A. S., Clarke T. E., 2011, *AJ*, 141, 149
- Cohen A. S., Lane W. M., Cotton W. D., Kassim N. E., Lazio T. J. W., Perley R. A., Condon J. J., Erickson W. C., 2007, *AJ*, 134, 1245
- Condon J. J., Broderick J. J., Seielstad G. A., Douglas K., Gregory P. C., 1994, *AJ*, 107, 1829
- Condon J. J., Cotton W. D., Greisen E. W., Yin Q. F., Perley R. A., Taylor G. B., Broderick J. J., 1998, *AJ*, 115, 1693
- Cowie L. L., Hu E. M., Jenkins E. B., York D. G., 1983, *ApJ*, 272, 29
- Crawford C. S., Allen S. W., Ebeling H., Edge A. C., Fabian A. C., 1999, *MNRAS*, 306, 857
- Croton D. J. et al., 2006, *MNRAS*, 365, 11
- De Breuck C., Tang Y., de Bruyn A. G., Röttgering H., van Breugel W., 2002, *A&A*, 394, 59
- de Vries W. H., Hodge J. A., Becker R. H., White R. L., Helfand D. J., 2007, *AJ*, 134, 457
- Dexter J., McKinney J. C., Markoff S., Tchekhovskoy A., 2014, *MNRAS*, 440, 2185
- Dicken D., Tadhunter C., Morganti R., Buchanan C., Oosterloo T., Axon D., 2008, *ApJ*, 678, 712
- Disney M., Wall J., 1977, *MNRAS*, 179, 235
- Done C., Gierlinski M., Kubota A., 2007, *A&AR*, 15, 1
- Dong R., Rasmussen J., Mulchaey J. S., 2010, *ApJ*, 712, 883
- Douglas J. N., Bash F. N., Bozyan F. A., Torrence G. W., Wolfe C., 1996, *AJ*, 111, 1945
- Dunn R. J. H., Fabian A. C., 2008, *MNRAS*, 385, 757
- Dutson K. L., Edge A. C., Hinton J. A., Hogan M. T., Gurwell M. A., Alston W. N., 2014, *MNRAS*, 442, 2048
- Ebeling H., Edge A. C., Böhringer H., Allen S. W., Crawford C. S., Fabian A. C., Voges W., Huchra J. P., 1998, *MNRAS*, 301, 881
- Ebeling H., Edge A. C., Allen S. W., Crawford C. S., Fabian A. C., Huchra J. P., 2000, *MNRAS*, 318, 333
- Ebeling H., Edge A. C., Mantz A., Barrett E., Henry J. P., Ma C. J., van Speybroeck L., 2010, *MNRAS*, 407, 83
- Edge A. C., 2001, *MNRAS*, 328, 762
- Edge A. C., Stewart G. C., Fabian A. C., Arnaud K. A., 1990, *MNRAS*, 245, 559
- Egami E. et al., 2006, *ApJ*, 647, 922
- Ekers R. D., Simkin S. M., 1983, *ApJ*, 265, 85
- Fabian A. C., 1994, *ARA&A*, 32, 277
- Fabian A. C., 2012, *ARA&A*, 50, 455
- Fabian A. C. et al., 2000, *MNRAS*, 318, L65
- Fabian A. C., Reynolds C. S., Taylor G. B., Dunn R. J. H., 2005, *MNRAS*, 363, 891
- Fanti C., Fanti R., De Ruiter H. R., Parma P., 1986, *ApJS*, 65, 145
- Feain I. J. et al., 2009, *ApJ*, 707, 114
- Fender R., 2001, *MNRAS*, 322, 31
- Ferretti L., Giovannini G., Govoni F., Murgia M., 2012, *A&AR*, 20, 54
- Ferland G. J., Fabian A. C., Hatch N. A., Johnstone R. M., Porter R. L., van Hoof P. A. M., Williams R. J. R., 2009, *MNRAS*, 392, 1475
- Ferrari C., Govoni F., Schindler S., Bykov A. M., Rephaeli Y., 2008, *Space Sci. Rev.*, 134, 93
- Fomalont E. B., Frey S., Paragi Z., Gurvits L. I., Scott W. K., Taylor A. R., Edwards P. G., Hirabayashi H., 2000, *ApJS*, 131, 95
- Franzen T. M. et al., 2014, *MNRAS*, 439, 1212
- Fujita Y., Suzuki T. K., 2005, *ApJ*, 630, L1
- Gaspari M., Brighenti F., Temi P., 2015, *A&A*, 579, A62
- Gaspari M., Ruszkowski M., Sharma P., 2012, *ApJ*, 746, 94
- Gentile G., Rodriguez C., Taylor G. B., Giovannini G., Allen S. W., Lane W. M., Kassim N. E., 2007, *ApJ*, 659, 225
- Giacintucci S., Venturi T., Murgia M., Dallacasa D., Athreya R., Bardelli S., Mazzotta P., Saikia D. J., 2007, *A&A*, 476, 99
- Giacintucci S. et al., 2011a, *ApJ*, 732, 95
- Giacintucci S., Markevitch M., Brunetti G., Cassano R., Venturi T., 2011b, *A&A*, 525, L10
- Giacintucci S., Markevitch M., Venturi T., Clarke T. E., Cassano R., Mazzotta P., 2014a, *ApJ*, 781, 9
- Giacintucci S., Markevitch M., Brunetti G., Zuhone J. A., Venturi T., Mazzotta P., Bourdin H., 2014b, *ApJ*, 795, 73
- Gitti M., Brunetti G., Setti G., 2002, *A&A*, 386, 456
- Gitti M., Ferretti L., Schindler S., 2006, *A&A*, 448, 853
- Gitti M., Ferrari C., Domainko W., Ferretti L., Schindler S., 2007, *A&A*, 470, L25
- Govoni F., Ferretti L., Giovannini G., Böhringer H., Reiprich T. H., Murgia M., 2001, *A&A*, 376, 803
- Gregory P. C., Condon J. J., 1991, *ApJS*, 75, 1011
- Greisen E. W., 2003, in Heckman A., ed., *Astrophysics and Space Science Library*, Vol. 285, *Information Handling in Astronomy – Historical Vistas*. Kluwer, Dordrecht, p. 109
- Griffith M. R., Wright A. E., 1993, *AJ*, 105, 1666
- Griffith M. R., Wright A. E., Burke B. F., Ekers R. D., 1994, *ApJS*, 90, 179
- Griffith M. R., Wright A. E., Burke B. F., Ekers R. D., 1995, *ApJS*, 97, 347
- Hamer S. L. et al., 2014, *MNRAS*, 437, 862
- Hardcastle M. J., Sakelliou I., 2004, *MNRAS*, 349, 560
- Harwood J. J., Hardcastle M. J., Croston J. H., Goodger J. L., 2013, *MNRAS*, 435, 3353
- Healey S. E., Romani R. W., Taylor G. B., Sadler E. M., Ricci R., Murphy T., Ulvestad J. S., Winn J. N., 2007, *ApJS*, 171, 61
- Heckman T. M., Best P. N., 2014, *ARA&A*, 52, 589
- Heckman T. M., Baum S. A., van Breugel W. J. M., McCarthy P., 1989, *ApJ*, 338, 48
- Heeschen D. S., Wade C. M., 1964, *AJ*, 69, 277
- Hlavacek-Larrondo J., Fabian A. C., Edge A. C., Ebeling H., Sanders J. S., Hogan M. T., Taylor G. B., 2012a, *MNRAS*, 421, 1360
- Hlavacek-Larrondo J., Fabian A. C., Edge A. C., Hogan M. T., 2012b, *MNRAS*, 424, 224
- Hlavacek-Larrondo J., Fabian A. C., Edge A. C., Ebeling H., Allen S. W., Sanders J. S., Taylor G. B., 2013, *MNRAS*, 431, 1638
- Hogan M. T., 2014, *The Radio Properties of Brightest Cluster Galaxies*, Durham theses, Durham University. Available at Durham E-Theses
- Hogan M. T., 2015, *MNRAS*, 453, 1223
- Jetha N. N., Hardcastle M. J., Sakelliou I., 2006, *MNRAS*, 368, 609
- Jones P. A., McAdam W. B., 1992, *ApJS*, 80, 137
- Kellermann K. I., Pauliny-Toth I. I. K., Williams P. J. S., 1969, *ApJ*, 157, 1
- Kempner J. C., Blanton E. L., Clarke T. E., Enßlin T. A., Johnston-Hollitt M., Rudnick L., 2004, in Reiprich T., Kempner J., Soker N., eds, *Proceedings*

- of the Riddle of Cooling Flows in Galaxies and Clusters of Galaxies. (available at <http://www.astro.virginia.edu/coolflow/proc.php>)
- Kharb P., Gabuzda D. C., O'Dea C. P., Shastri P., Baum S. A., 2009, *ApJ*, 694, 1485
- Knox L., Holder G. P., Church S. E., 2004, *ApJ*, 612, 96
- Labiano A., 2009, *Astron. Nachr.*, 330, 241
- Laing R. A., Bridle A. H., 2014, *MNRAS*, 437, 3405
- Lara L., Giovannini G., Cotton W. D., Feretti L., Venturi T., 2004, *A&A*, 415, 905
- Large M. I., Mills B. Y., Little A. G., Crawford D. F., Sutton J. M., 1981, *MNRAS*, 194, 693
- Laurent-Muehleisen S. A., Kollgaard R. I., Ryan P. J., Feigelson E. D., Brinkmann W., Siebert J., 1997, *A&AS*, 122, 235
- Li Y., Bryan G. L., 2014, *ApJ*, 789, 54
- Lim J., Leon S., Combes F., Dinh-V-Trung, 2000, *ApJ*, 545, L93
- Lin Y., Mohr J. J., 2007, *ApJS*, 170, 71
- Lin Y., Partridge B., Pober J. C., Boucheffry K. E., Burke S., Klein J. N., Coish J. W., Huffenberger K. M., 2009, *ApJ*, 694, 992
- Liuzzo E., Giovannini G., Giroletti M., Taylor G. B., 2009, *A&A*, 505, 509
- Liuzzo E., Giovanni G., Giroletti M., Taylor G. B., 2010, *A&A*, 516, A1
- Ly C., Walker R. C., Wrobel J. M., 2004, *AJ*, 127, 119
- Ma C. J., McNamara B. R., Nulsen P. E. J., 2013, *ApJ*, 763, 63
- McDonald M. et al., 2013a, *ApJ*, 774, 23
- McDonald M., Bayliss M., Benson B. A., 2013b, *Nature*, 488, 349
- McNamara B. R., Nulsen P. E. J., 2007, *ARA&A*, 45, 117
- McNamara B. R., Nulsen P. E. J., 2012, *New J. Phys.*, 14, 055023
- McNamara B. R. et al., 2000, *ApJ*, 534, L135
- McNamara B. R., Rohanizadegan M., Nulsen P. E. J., 2011, *ApJ*, 727, 39
- McNamara B. R. et al., 2014, *ApJ*, 785, 44
- Magorrian J. et al., 1998, *AJ*, 115, 2285
- Maiolino R., Rieke G. H., 1995, *ApJ*, 454, 9511
- Mason B. S., Weintraub L., Sievers J., Bond J. R., Myers S. T., Pearson T. J., Readhead A. C. S., Shepherd M. C., 2009, *ApJ*, 704, 1433
- Mauch T., Murphy T., Buttery H. J., Curran J., Hunstead R. W., Piestrzynska B., Robertson J. G., Sadler E. M., 2003, *MNRAS*, 342, 1117
- Million E. T., Allen S. W., 2009, *MNRAS*, 399, 1307
- Mirabel I. F., Rodríguez L. F., 1994, *Nature*, 371, 46
- Mirabel I. F., Rodríguez L. F., Cordier B., Paul J., Lebrun F., 1992, *Nature*, 358, 215
- Mittal R., Hudson D. S., Reiprich T. H., Clarke T., 2009, *A&A*, 501, 835
- Murphy T. et al., 2010, *MNRAS*, 402, 2403
- Nagar N. M., Falcke H., Wilson A. S., 2005, *A&A*, 435, 521
- O'Dea C. P., 1998, *PASP*, 110, 493
- O'Dea C. P. et al., 2008, *ApJ*, 681, 1035
- Orienti M., Dallacasa D., 2014, *MNRAS*, 438, 463
- O'Sullivan E., Vrtillek J. M., Harris D. E., Ponman T. J., 2007, *ApJ*, 658, 299
- Owen F. N., Eilek J. A., Kassim N. E., 2000, *ApJ*, 543, 611
- Panagoulia E. K., Fabian A. C., Sanders J. S., 2014, *MNRAS*, 438, 2341
- Parma P., Murgia M., de Ruiter H. R., Fanti R., Mack K.-H., Govoni F., 2007, *A&A*, 470, 875
- Peres C. B., Fabian A. C., Edge A. C., Allen S. W., Johnstone R. M., White D. A., 1998, *MNRAS*, 298, 416
- Perley R. A., Butler B. J., 2013, *ApJS*, 204, 19
- Peterson J. R., Kahn S. M., Paerels F. B. S., Kaastra J. S., Tamura T., Bleeker J. A. M., Ferrigno C., Jernigan J. G., 2003, *ApJ*, 590, 207
- Petrov L., 2011, *AJ*, 142, 105
- Pfrommer C., Enßlin T. A., 2003, *A&A*, 407, L73
- Pimblet K. A., Smail I., Edge A. C., O'Hely E., Couch W. J., Zabludoff A. I., 2006, *MNRAS*, 366, 645
- Pizzolato F., Soker N., 2005, *ApJ*, 632, 821
- Quillen A. C. et al., 2008, *ApJS*, 176, 39
- Rafferty D. A., McNamara B. R., Nulsen P. E. J., 2008, *ApJ*, 687, 899
- Randall S. W. et al., 2011, *ApJ*, 726, 86
- Rawlings S., Saunders R., Eales S. A., Mackay C. D., 1989, *MNRAS*, 240, 701
- Rector T. A., Stocke J. T., Perlman E. S., 1999, *ApJ*, 516, 145
- Reiprich T. H., Böhringer H., 2002, *ApJ*, 567, 716
- Remillard R. A., McClintock J. E., 2006, *Am. Astron. Soc. Meeting*, 209, 0705
- Rengelink R. B., Tang Y., de Bruyn A. G., Miley G. K., Bremer M. N., Roettgering H. J. A., Bremer M. A. R., 1997, *A&AS*, 124, 259
- Reynolds J. E., 1994, *A Revised Flux Scale for the AT Compact Array*. ATNF Memo AT/39.3/040
- Roettgering H. J. A., Lacy M., Miley G. K., Chambers K. C., Saunders R., 1994, *A&AS*, 108, 79
- Russell H. R., McNamara B. R., Edge A. C., Hogan M. T., Main R. A., Vantyghem A. N., 2013, *MNRAS*, 432, 530
- Russell H. R. et al., 2014, *ApJ*, 784, 78
- Sadler E. M., Ricci R., Ekers R. D., Sault R. J., Jackson C. A., de Zotti G., 2008, *MNRAS*, 385, 1656
- Sadler E. M., Ekers R. D., Mahony E., Mauch T., Murphy T., 2014, *MNRAS*, 438, 796
- Salome P., Combes F., 2003, *A&A*, 412, 6574
- Samuele R., McNamara B. R., Vikhlinin A., Mullis C. R., 2011, *ApJ*, 731, 31
- Sanders J. S., Fabian A. C., 2011, *MNRAS*, 412, L35
- Sanderson A. J. R., Edge A. C., Smith G. J., 2009, *MNRAS*, 398, 1698
- Santos J. S., Tozzi P., Rosati P., Böhringer H., 2010, *A&A*, 521, A64
- Sault R. J., Teuben P. J., Wright M. C. H., 1995, in Shaw R. A., Payne H. E., Hayes J. J. E., eds, *ASP Conf. Ser. Vol. 77, Astronomical Data Analysis Software and Systems IV*. Astron. Soc. Pac., San Francisco, p. 433
- Silk J., Rees M. J., 1998, *A&A*, 331, L1
- Simkin S. M., 1979, *ApJ*, 234, 56
- Slee O. B., 1995, *Aust. J. Phys.*, 48, 143
- Slee O. B., Sadler E. M., Reynolds J. E., Ekers R. D., 1994, *MNRAS*, 269, 928
- Slee O. B., Roy A. L., Murgia M., Andernach H., Ehle M., 2001, *AJ*, 122, 1172
- Stott J. P. et al., 2012, *MNRAS*, 422, 2213
- Sun M., Voit G. M., Donahue M., Jones C., Forman W., Vikhlinin A., 2009, *ApJ*, 693, 1142
- Tadhunter C. N., Morganti R., Robinson A., Dickson R., Villar-Martin M., Fosbury R. A. E., 1998, *MNRAS*, 298, 1035
- Taylor G. B., 1996, *ApJ*, 470, 394
- Taylor G. B., O'Dea C. P., Peck A. B., Koekemoer A. M., 1999, *ApJ*, 512, L27
- Taylor G. B., Sanders J. S., Fabian A. C., Allen S. W., 2006, *MNRAS*, 365, 705
- Tingay S. J. et al., 2013, *Publ. Astron. Soc. Aust.*, 30, 7
- Tremaine S., 1990, in Wielen R., ed., *Proc. Int. Conf., Dynamics and Interactions of Galaxies*. Springer-Verlag, Berlin, p. 394
- van Haarlem M. P. et al., 2013, *A&A*, 556, A2
- van Weeren R. J., Röttgering H. J. A., Brüggem M., 2011, *A&A*, 527, A114
- Venturi T., Dallacasa D., Stefanachi F., 2004, *A&A*, 422, 515
- Voigt L. M., Fabian A. C., 2004, *MNRAS*, 347, 1130
- Voit G. M., Donahue M., 2015, *ApJ*, 799, L1
- WalDRAM E. M., Yates J. A., Riley J. M., Warner P. J., 1996, *MNRAS*, 282, 779
- Walker S. A., Fabian A. C., Sanders J. S., 2014, *MNRAS*, 441, L31
- Werner N. et al., 2014, *MNRAS*, 439, 2291
- White R. L., Becker R. H., Helfand D. J., Gregg M. D., 1997, *ApJ*, 475, 479
- Williamson R. et al., 2011, *ApJ*, 738, 139
- Willott C. J., Rawlings S., Blundell K. M., Lacy M., 1999, *MNRAS*, 309, 1017
- Wilman R. J., Edge A. C., Johnstone R. M., 2005, *MNRAS*, 359, 755
- Wislon W. E. et al., 2011, *MNRAS*, 416, 832
- Wright A., Otrupcek R., 1990, *PKS Catalog*, 0
- Wright A. E., Griffith M. R., Burke B. F., Ekers R. D., 1994, *ApJS*, 91, 111
- ZuHone J. A., Markevitch M., Brunetti G., Giacintucci S., 2013, *ApJ*, 762, 78

SUPPORTING INFORMATION

Additional Supporting Information may be found in the online version of this article:

Appendix.

(<http://mnras.oxfordjournals.org/lookup/suppl/doi:10.1093/mnras/stv1517/-/DC1>).

Please note: Oxford University Press is not responsible for the content or functionality of any supporting materials supplied by the authors. Any queries (other than missing material) should be directed to the corresponding author for the paper.

This paper has been typeset from a \TeX/L\AA\TeX file prepared by the author.